ISSN 1883 - 0323

TOHOKU UNIVERSITY

IMR KINKEN Research Highlights 2026

Institute for Materials Research, Tohoku University

Research

KINKEN

Research Highlights

2026

Institute for Materials Research, Tohoku University

KINKEN Research Highlights 2026

Contents

G : GIMRT (Global Institute for Materials Research Tohoku) is a program in which researchers from inside and outside the institute conduct joint research based on a common research theme.

I : International Co-Authored Paper

2. Energy-Related Materials

3. Electronic Materials

Research Centers

Research

Preface

Dear Colleagues,

We are delighted to present “KINKEN Research Highlights 2026,” our annual report that showcases research findings from the Institute for Materials Research (IMR) at Tohoku University for the past year. KINKEN is the abbreviation for “Kinzoku Zairyo Kenkyusho,” the Japanese name for IMR, and is well known in the materials science community.

IMR has a rich history spanning over one hundred years since its establishment in 1916. Initially, the focus was on iron and steel materials, but as times changed and research progressed, its scope expanded to include the fundamentals and applications of various materials, including non-metals such as semiconductors and ceramics. With these changes, the institute changed its name from the Research Institute for Iron, Steel and Other Metals (RIISOM) to the current one in 1987. Ever since Dr. Kotaro Honda, its first director, invented the world’s first artificial permanent magnet called KS magnet steel, the institute has developed many new materials for practical use, including Sendust alloy, SiC fibers, and soft magnetic amorphous alloys, and has also conducted not only fundamental research, but also pioneering research in the search for new materials and the elucidation of physical properties such as magnetism and superconductivity. It has become a global center in materials science.

A key feature of IMR is its integration of fundamental and applied research, as well as science and engineering fields. Additionally, the institute stands out for its joint research with both domestic and international researchers, utilizing world-class facilities for experiments (high-energy irradiation testing, high magnetic fields, supercomputers, etc.) and for the creation and evaluation of new materials. In

Takahiko Sasaki

Director Prof. Takahiko Sasaki

2018, IMR was certified as the International Joint Usage/Research Center for Materials Science, known as “Global Institute for Materials Research Tohoku” (GIMRT). IMR is committed to further promoting research and fostering the next generation of researchers, and putting into practice Dr. Honda’s words, “Industry is the training ground of academics,” it also focuses on the likes of industry-academia collaboration and engineer training.

IMR is committed to creating a sustainable society, a goal shared by the global community. Its materials science research has the power not only to solve issues but also to positively transform society. The institute is dedicated to supporting the international competitiveness of Japan’s materials manufacturing and engaging in global endeavors to create academic intellectual property shared by humankind. IMR will continue to work on innovative materials science research that will bring about a paradigm shift with a long-term vision and contribute to developing human resources who will lead the future.

We hope KINKEN Research Highlights will provide insights into our recent research activities and help encourage worldwide collaboration with IMR. We value your continued support and welcome any suggestions.

Infrastructural Materials

IMR KINKEN Research Highlights 2026

Alloying Effects On Spinodal Decomposition Induced Nano-Sized X-N Clustering During Low-Temperature Nitriding of Austenitic Fe-35Ni-X Alloys

The addition of nitride-forming elements such as Cr is vital for the formation of the expanded austenite supersaturated by nitrogen (N) during low-temperature nitriding of austenitic steels. In the present work, the effect of different nitride-forming element addition on the low-temperature nitriding behavior and nanostructure evolution is systematically investigated for austenitic Fe-35Ni-10X (at%) alloys.

The surface formation of expanded austenite during the low temperature (~673 K) nitriding of Fe-Ni-Cr austenitic alloys is capable of surface hardening without sacrificing the corrosion resistance of the material. Such expanded austenite is conventionally regarded as a nitrogen-supersaturated fcc solid solution with Cr-N short-range ordering. However, Cr-N clustering in expanded austenite promoted by Cr-N attractive interaction was recently reported for low-temperature nitrided Fe-35Ni-Cr alloys [1-2].

In the present work, Fe-35Ni-10X (X=Al, Mn, Mo, Cr, V) alloys were subjected to low-temperature plasma nitriding at 673 K for 30 h. The effect of nitride-forming element X addition on the low-temperature nitriding behavior and nanostructure evolution of expanded austenite is systematically investigated to quantitatively clarify the effect of the interaction between X and N [3]. The addition of X promotes nitrogen absorption, lattice expansion and thus hardening effect for the expanded austenite layers in the order of X-N attractive interaction, i.e. 10Mn< 10Al< 10Mo< 10Cr< 10V, as shown in Fig. 1. Compared with the microhardness of Fe-N retained austenite, the expanded austenite layers in the 10Mo and 10Cr alloys were much harder despite having a similar N content, indicating the existence of hardening factors other than N concentration.

The nano-sized X-N (X=Mo, Cr, V) clusters were directly revealed in the expanded austenite layers as strong <001>γ streaks in selected area diffraction, obvious modulated structure along <010>γ in TEM and simultaneous enrichment of X and N and rejection of Fe, Ni inside the clusters observed by 3DAP (Fig. 2). The chemical driving force, strain energy and modulation wavelength for coherent spinodal decomposition were calculated thermodynamically under multi-compositional concentration fluctuations. Our calculation confirmed that the observed X-N clustering for the 10Mo, 10Cr and 10V alloys was induced by spinodal decomposition and becomes possible when both fluctuations of X and N are involved, and the enrichment of X and N occurs simultaneously and equally. Consistent with the results

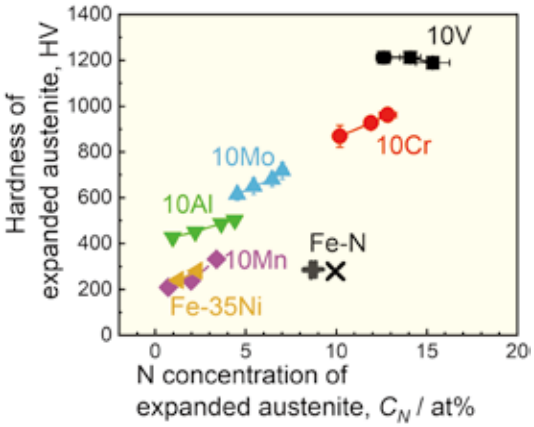

Fig. 1 The relationship between the N concentration and the hardness of expanded austenite layers for Fe-35Ni-10X (X=Mo, Cr, V) alloys nitrided at 673 K for 30 h [3].

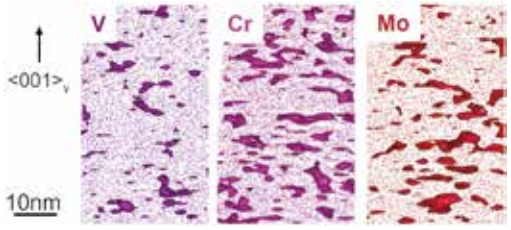

Fig. 2 3DAP atom maps with highlighted iso-surfaces showing X-N clusters of the nitrided 10X alloys [3].

shown in TEM and 3DAP, the calculated driving force for such multi-compositional spinodal decomposition increases in the order of X-N attractive interaction. The calculated results for the spinodal wavelength agreed well with the experimental results as the wavelength increases in the order of 10V< 10Cr< 10Mo.

References

[1] Y. Xie, G. Miyamoto, and T. Furuhara, Scr. Mater. **213**, 114637 (2022).

[2] Y. Xie, G. Miyamoto, and T. Furuhara, Acta Mater. **253**, 118921 (2023).

[3] Y. Xie, G. Miyamoto, Y. Hayasaka, and T. Furuhara, Acta Mater. **301**, 121543 (2025).

Yulin Xie, Goro Miyamoto, Yuichiro Hayasaka, and Tadashi Furuhara (Microstructure Design of Structural Metallic Materials Research Laboratory)
E-mail: yulin.xie.d1@tohoku.ac.jp
URL: https://www.st-mat.imr.tohoku.ac.jp/en/index.html

GIMRT

Large-Scale Molecular Dynamics Simulation for the Design of Nanomaterials and Highly Functional Materials

To develop nanomaterials and highly functional materials, a comprehensive understanding of multiphysics phenomena—including chemical reactions, friction, stress, and fluid dynamics—is essential. We employed coarse-grained molecular dynamics and reactive molecular dynamics simulations to investigate these phenomena, with the aim of advancing materials and system design.

The development of nanomaterials and highly functional materials is essential across many fields. Achieving this goal requires a deep understanding of multiphysics phenomena, including chemical reactions, friction, stress, and fluid dynamics. Advances in high-performance computing have made it possible to simulate these processes at the atomic scale. In this context, we have employed coarse-grained molecular dynamics and reactive molecular dynamics simulations to advance next-generation materials design [1,2].

Metal and metal oxide nanoparticles possess unique optical, electronic, and catalytic properties, and their surfaces are often modified with organic ligands to maintain dispersion. However, the dispersibility of organically modified nanoparticles (OMNPs) cannot be fully explained by solubility parameters. Although OMNPs disperse well in hexane, they aggregate in decane despite similar solubility parameters. Molecular dynamics simulations show that hexane molecules orient randomly, whereas decane molecules align parallel to the ligands, penetrate the ligand shells, and form bridge structures that promote aggregation (Fig. 1). These findings indicate that nanoscale interfacial structures, strongly influenced by solvent molecular shape, play an essential role in determining OMNP dispersibility [1].

Silicon carbide (SiC) exhibits low friction in aqueous environments due to the formation of a tribolayer through tribochemical reactions. Although this layer is typically extremely thin and is quickly worn away, the low-friction state is nevertheless maintained in experiments. To clarify this behavior, we performed molecular dynamics sliding simulations of the SiC water system (Fig. 2). The results show that tribochemical reactions between amorphous SiC (a-SiC) and water generate a tribolayer composed of a silica-based layer and a carbon layer. The formation of the silica-based layer sustains hydrodynamic lubrication, while the carbon layer suppresses adhesion. However, excessive coverage by the carbon layer disrupts the continuous formation of the tribolayer. We found that an uneven distribution of chemical bonds in amorphous SiC is crucial, as it enables the simultaneous and continuous formation of both layers, thereby maintaining a low-friction state [2].

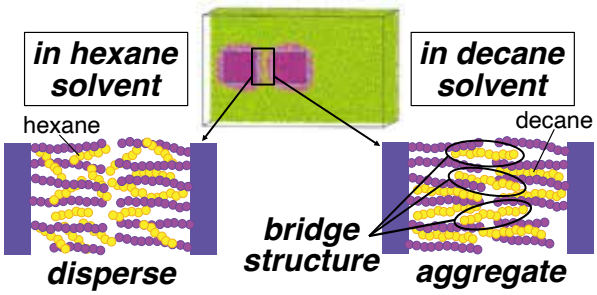

Fig. 1 Schematic illustration of the differing dispersibility of OMNPs in hexane and decane solvents. Reproduced from Ref. [1] under the CC BY 4.0 license.

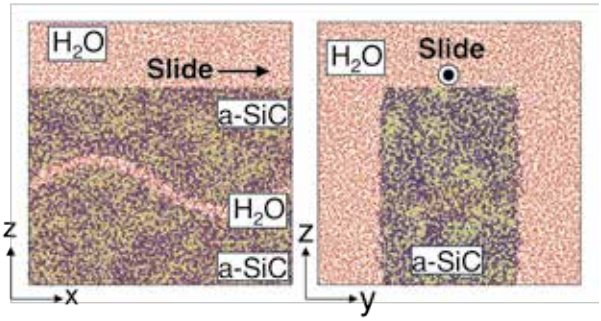

Fig. 2 Sliding simulation model of a-SiC in water, enabling us to investigate the continuous formation process of the tribolayer.

References

[1] Y. Ootani, R. Taniai, K. Jojima, M. Nakamura, S. Fukushima, N. Ozawa, and M. Kubo, ACS Appl. Nano. Mater. **8**, 12353 (2025).
[2] M. Kawaura, Y. Ootani, S. Fukushima, Y. Su, N. Ozawa, K. Adachi, and M. Kubo, Tribol. Int. **206**, 110570 (2025).

Momoji Kubo (Materials Design by Computer Simulation Research Laboratory)
E-mail: momoji@tohoku.ac.jp
URL: http://www.simulation.imr.tohoku.ac.jp/eng/index.html

Observation of Coherency-Dependent Hydrogen Diffusion at Σ3 Grain Boundaries in Pure Ni

Hydrogen embrittlement refers to the ductility loss of metals caused by transport and accumulation of hydrogen atoms. This study visualized hydrogen diffusion at Σ3 grain boundaries (GBs) and clarified that hydrogen diffusion at coherent Σ3 GBs is identical with the grain interior, whereas incoherent Σ3 GBs exhibit enhanced hydrogen diffusion governed by deviation angle.

Hydrogen embrittlement is the loss of ductility caused by hydrogen atoms in metals. When face-centered cubic (fcc) metals such as Ni alloys lose their ductility due to hydrogen, intergranular fracture is often observed. This indicates that GBs play a key role in hydrogen transport and localization.

Σ3 GBs are commonly regarded as mechanically beneficial. Increasing the fraction of Σ3 GBs is considered an effective strategy for mitigating hydrogen embrittlement. However, hydrogen-related cracking at Σ3 GBs has been reported, implying that the hydrogen diffusion behavior is different among Σ3 GBs.

In this study, hydrogen diffusion at Σ3 GBs in pure Ni was observed using a polymer-based hydrogen sensor. The polymeric sensors enable real-time visualization of hydrogen flux distribution in metals [1-5]. Figure 1a shows the optical image of the sensor [1]. The sensor is originally dark blue and gets brighter when it reacts with hydrogen atoms [2-4]. After removing the sensor, a backscattered electron (BSE) image of the same area was taken (Fig. 1b). Both white dashed lines in Fig. 1b represent coherent Σ3 GBs with a deviation angle of 2°. Because the crystal structure of coherent Σ3 GBs was almost the same as that of the grain interior, brightness change (enhanced hydrogen diffusion) was barely observed.

The Σ3 GBs indicated by the yellow arrows showed the enhanced hydrogen diffusion. One of the GBs was an incoherent Σ3 GB with a deviation angle of 24°, while the other was coherent. Figure 1c and 1d show enlarged views of the GBs indicated by the yellow arrows in Fig. 1a and 1b. Figure 1e shows the contour map of the brightness change (ΔY) of the sensor. The green and white dashed lines indicate incoherent and coherent Σ3 GBs, respectively. Figure 1e showed that enhanced hydrogen diffusion occurred at the nano-scale incoherent portions of the Σ3 GB.

A statistical analysis of hydrogen flux revealed the following order: high-angle random GBs > incoherent Σ3 GBs > low-angle GBs > coherent Σ3 GBs ≈ grain interior. This study clarified that hydrogen diffusion along GBs in pure Ni depends on GB character and coherency.

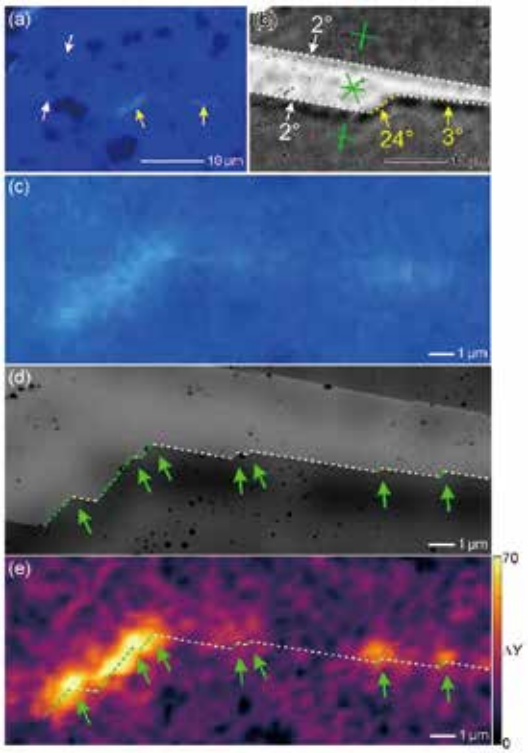

Fig. 1 (a) Optical image of the hydrogen sensor and (b) BSE image of the corresponding area. The deviation angle of each boundary is shown in degrees. (c) Enlarged optical image and (d) BSE image of the GB indicated by the yellow arrows in (b). The green and white dashed lines indicate the incoherent and coherent portions of the Σ3 GB, respectively. (e) Contour map of brightness change of the sensor. Enhanced hydrogen diffusion was confirmed at the incoherent portions [1].

References

[1] H. Kakinuma, M. Koyama, R.S. Varanasi, S. Ajito, and E. Akiyama, Mater. Res. Lett. **13**, 357 (2025).
[2] H. Kakinuma, S. Ajito, K. Okumura, M. Akahoshi, Y. Takabatake, T. Omura, M. Koyama, and E. Akiyama, Corros. Sci. **258**, 113386 (2026).
[3] H. Kakinuma, S. Ajito, M. Koyama, and E. Akiyama, Mater. Trans. **66**, 1095 (2025).
[4] Z. Wang, S. Ajito, Y. Wang, M. Koyama, E. Akiyama, and H. Kakinuma, Npj Mater. Degrad. **9**, 78 (2025).
[5] H. Kakinuma, Y. Sasaki, S. Ajito, M. Koyama, and E. Akiyama, ISIJ. Int., ISIJINT-2025-340 (2025).

Hiroshi Kakinuma (Environmentally Robust Materials Research Laboratory)
E-mail: hiroshi.kakinuma.a1@tohoku.ac.jp
URL: https://akiyamaimr-e.amebaownd.com/

GIMRT

Synthesis of FeCr-Mg Multi-Heterostructures via Liquid Metal Dealloying and Subsequent Y/Al Alloying

This study developed hierarchical FeCr–Mg multi-heterostructures through dealloying followed by Y or Al addition. Distinct microstructural evolutions—secondary phases for Y and ligament modification for Al—resulted in superior mechanical properties compared to unimodal composites, highlighting the potential of this sequential alloying strategy

Conventional metal matrix composites often face trade-offs between strength and ductility due to poor interfacial bonding. To address this, this study evaluates the microstructural evolution and mechanical enhancement of FeCr–Mg composites synthesized via a novel strategy combining Liquid Metal Dealloying (LMD) and subsequent alloying [1]. LMD serves as the foundational process, creating a 3D bicontinuous scaffold through the selective dissolution of Ni from an $(Fe_{80}Cr_{20})_{50}Ni_{50}$ precursor in a pure Mg melt. The resulting 3D interconnected FeCr–Mg composite was subsequently immersed in $Mg_{90}Y_{10}$ or $Mg_{90}Al_{10}$ melts to induce specific alloying reactions, as suggested by the interatomic interactions shown in Fig.1(a).

The subsequent alloying step induced divergent microstructural evolutions depending on the alloying element. Yttrium addition proved relatively inert towards the FeCr ligaments, reacting instead to form secondary plate-shaped $Mg_{25}Y_4$ intermetallic phases within the soft Mg matrix. In contrast, aluminum addition triggered significant structural modifications as illustrated in Fig.1(b). It formed a thick Al-alloyed layer and an ordered B2 phase within the ligaments and acted as a heterogeneous nucleation site. This nucleation mechanism refined the matrix into Mg nanograins containing a fine lamellar β-$Mg_{17}Al_{12}$ phase, establishing a complex hierarchical structure as shown in Fig.2.

Consequently, the multi-heterostructures synthesized via subsequent alloying exhibited superior mechanical performance compared to the unimodal FeCr–Mg composite. The formation of the Al-alloyed layer increased the solid phase volume fraction, directly contributing to the highest yield strength and ultimate tensile strength. These findings demonstrate that subsequent alloying is a promising strategy for tailoring microstructure. Specifically, the Al-induced hierarchical heterogeneity offers a robust pathway for overcoming traditional trade-offs and enhancing the mechanical properties of advanced structural materials.

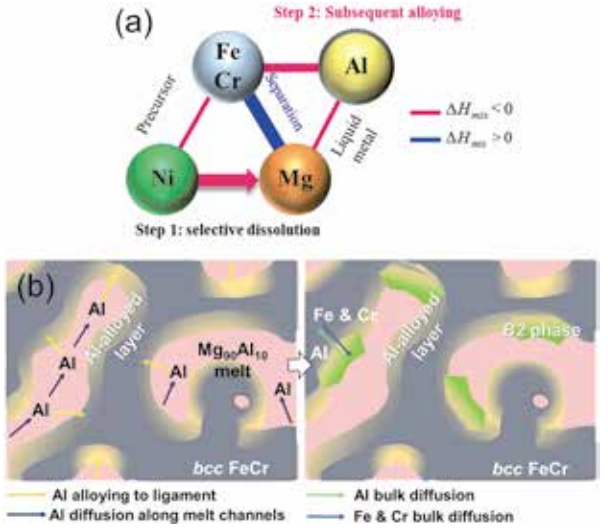

Fig. 1 (a) Reaction diagram of LMD and subsequent alloying. (b) Schematic of microstructural changes during Al alloying.

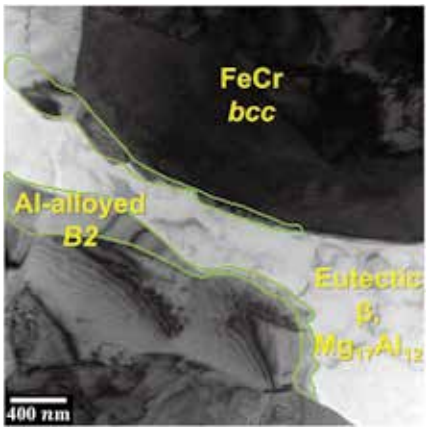

Fig. 2 TEM micrograph of the microstructure after Al alloying.

References

[1] Y.B. Jeong, T. Wada, J. Seong, G.H. Gu, H.S. Kim, S.-H. Joo, and H. Kato, Adv. Compos. Hybrid Mater. **8**, 373 (2025).

Hidemi Kato (Non-Equilibrium Materials Research Laboratory)
E-mail: hidemi.kato.b7@tohoku.ac.jp
URL: http://www.nem2.imr.tohoku.ac.jp/index-e.html

Enhancing Dislocation Strengthening in Face-Centered Cubic High-Entropy Alloys through Interstitial Nitrogen

Non-equiatomic high-entropy alloys (HEAs) featuring transformation-induced plasticity (TRIP) hold great potential as a novel class of structural materials. In this study, we demonstrate that a trace addition of nitrogen significantly enhances dislocation strengthening in a face-centered cubic (FCC) HEA, resulting in an excellent combination of high yield strength and ductility.

HEAs are generally defined as multi-principal element alloys composed of five or more elements in near-equimolar proportions (5–35 at %) [1]. The equiatomic CoCrFeMnNi HEA, known as the Cantor alloy, is one of the most widely studied HEAs [2]. This alloy exhibits a single-phase FCC microstructure and deforms plastically primarily through dislocation slip.

By contrast, Li et al. [3] integrated the TRIP effect into FCC HEAs by reducing the stacking fault energy (SFE) through chemical composition tuning. This approach achieved exceptional combinations of ultimate tensile strength (UTS) and ductility. However, the yield stress of these TRIP-assisted HEAs remains relatively low (<400 MPa), necessitating further strengthening for broader structural applications.

In this study, we investigated the synergistic effects of nitrogen addition and thermomechanical processing in a model $Co_{20}Cr_{20}Fe_{34}Mn_{20}Ni_6$ HEA [4]. The base N-free and N-doped (0.3 at.%) alloys were processed by hot-caliber rolling at 800 and 1000°C. The addition of nitrogen not only enhanced solid-solution strengthening but also led to a significant increase in overall strength (Fig. 1). Quantitative dislocation density analysis, performed via time-of-flight neutron diffraction measurements, revealed a monotonic increase in dislocation density with rolling reduction, which governs the overall strength of the hot-caliber-rolled alloys. Notably, the addition of trace nitrogen significantly increased the dislocation density to 1.6×10^{15} m^{-2} at 800°C (Fig. 2), which is attributed to the strong interactions between dislocations and interstitial nitrogen atoms. While higher rolling temperatures decreased the dislocation density due to dynamic recrystallization, as evidenced by the slight grain refinement, additional strengthening from planar defects was activated. Consequently, the hot-caliber-rolled N-doped alloys exhibit an exceptional combination of high yield stress (1 GPa), representing a four-fold increase compared to the base alloy, while maintaining 40% elongation-to-failure.

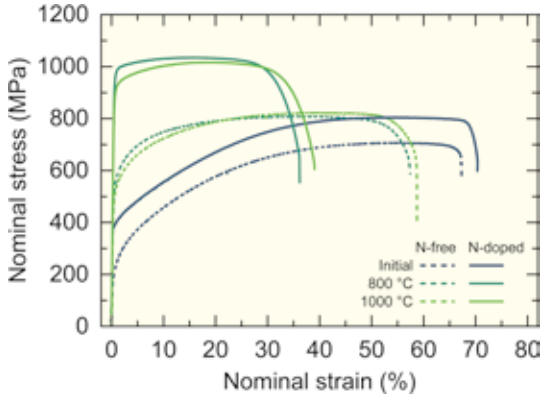

Fig. 1 Nominal stress–strain curves of the alloys after three-pass hot-caliber rolling.

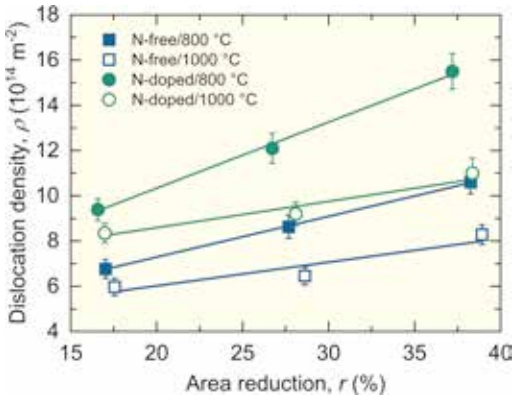

Fig. 2 Dislocation density of hot-caliber-rolled alloys determined by neutron diffraction

This study provides critical insights into the strengthening strategy at the intersection of alloy design and thermomechanical treatment.

References

[1] Y. Zhang, T. T. Zuo, Z. Tang, M.C. Gao, K.A. Dahmen, P.K. Liaw, and Z.P. Lu, Prog. Mater. Sci. **61**, 1 (2014).

[2] B. Cantor, I. T. H. Chang, P. Knight, and A. J. B. Vincent, Mater. Sci. Eng. A **375–377**, 213 (2004).

[3] Z. Li, K. G. Pradeep, Y. Deng, D. Raabe, and C. C. Tasan, Nature **534**, 227 (2016).

[4] K. Yamanaka, M. Mori, K. Yoshida, Y. Onuki, and S. Sato, Appl. Mater. Today **45**, 102834 (2025).

Kenta Yamanaka (Deformation Processing Research Laboratory)
E-mail: kenta.yamanaka.c5@tohoku.ac.jp
URL: http://www.imr.tohoku.ac.jp/en/about/divisions-and-centers/research-division/24.html

International Co-Authored Paper

Atomic-Level Characterization of Y Segregation Behavior in a Near Σ3 Boundary of Magnesium Aluminate Spinel

The grain boundary (GB) structure including atomic arrangements plays a crucial role in dictating the segregation behavior of solute species, which affect the mechanical and electrical properties. In this study, a near-Σ3 twist boundary was fabricated using spinel single crystals, and detailed atomic-level characterization was carried out using an aberration-corrected scanning transmission electron microscopy (STEM). An ordered Y segregation was found in some regions between the dislocation network as well as a disordered Y segregation was observed in the vicinity of the dislocation network.

Magnesium aluminate spinel (MAS, $MgAl_2O_4$) is a unique ceramic material that is transparent over a wide range from UV to mid-IR and presents enhanced toughness, which could be utilized for windows in extreme environments [1]. However, fracture failures tend to occur at GBs, which is one of the major limiting factors for practical MAS applications. A bicrystal was fabricated to be a Σ3 configuration and atomic-level characterization of the GB was performed to identify details of Y segregation behavior. For the atomic-level characterization by aberration-corrected STEM, electron transparent thin specimens in a pseudo plan-view and cross-section geometries were prepared by a focused ion beam (FIB) instrument.

Figure 1(a) shows an atomic-resolution STEM image of the pseudo plan view geometry of the near Σ3 GB. Hexagonal GB network formed sue to a slight deviation from the true Σ3 configuration can be seen. Ordered Y segregations can be seen in one of the hexagonal GB network domains surrounded by a cyan line. In addition, random Y segregation was also found around the hexagonal network domains [2, 3].

Figure 1(b) shows a representative micrograph of the same GB but observed from an orthogonal direction (along the [$\bar{1}$10] direction for the cross-sectional view). The size of the hexagonal region where Y atoms are highly ordered in Fig. 1(a) (cyan hexagon) matches the length of the segregated segment observed along the [$\bar{1}$10] zone axis [2, 3]. The hexagonal shape of the highly ordered segregation regions explains why the intensity of the ordered Y segregation along the [$\bar{1}$10] zone axis decreased towards the ends in Fig. 1(b).

A summary of the segregation behavior that occurred in the regions between the dislocation networks is presented in Fig. 2. The presence of dislocation network dictated the segregation behaviors at the GB. First, disordered Y segregation was found in the vicinity of the dislocation network. Second, ordered Y segregation was found in some regions between the dislocation network. Third, almost no Y segregation was found in the remaining regions between the dislocation network [3].

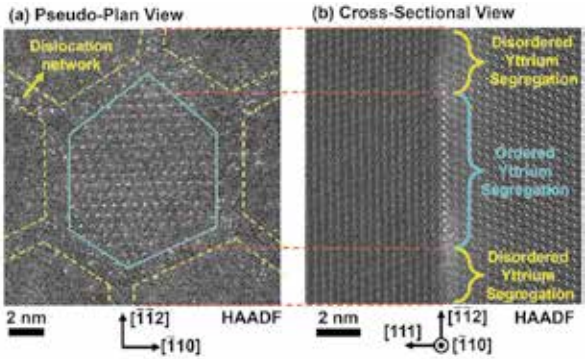

Fig. 1 Comparison of the (a) in-plane segregation behavior and (b) the projected segregation behavior along the [$\bar{1}$10] zone axis of the near Σ3 twist boundary.

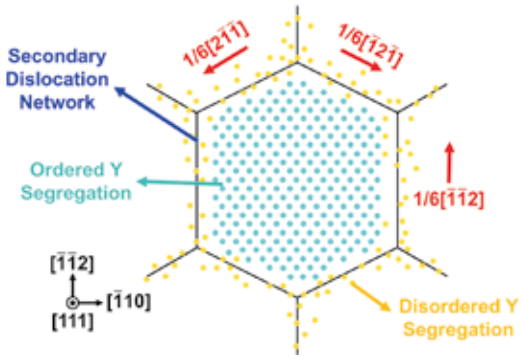

Fig. 2 A summary of Y segregation behavior in the near Σ3 twist boundary. The presence of dislocation network dictated the segregation behaviors at the boundary. First, disordered Y segregation was found in the vicinity of the dislocation network. Second, ordered Y segregation was found in some regions between the dislocation network. Third, almost no Y segregation was found in the remaining regions between the dislocation network.

References

[1] A. Campos-Quiros, M. Zughbi, A. Kundu, and M. Watanabe, J. Mater. Sci. **60**, 1-27 (2025).

[2] A. Campos-Quiros, A. Kundu, and M. Watanabe, Microsc. Microanal. **31**, Suppl 1, 1347–1348 (2025).

[3] A. Campos-Quiros, A. Kundu, and M. Watanabe, Acta Mater. **309**, 122107 (2026).

Masashi Watanabe (Analytical Science Research Laboratory)
E-mail: masashi.watanabe.d2@tohoku.ac.jp
URL: http://www.imr.tohoku.ac.jp/en/about/divisions-and-centers/research-division/27.html

Metal-Doped TiO_2 Nanosheets for Efficient Photocatalysis and Antibacterial Applications

TiO_2 nanomaterials are well-known for their effective photocatalytic properties, with broad practical applications. To suppress electron–hole recombination and enhance photocatalytic performance, we synthesized highly ordered TiO_2 nanosheets with exposed [001] facets and subsequently doped them with Ag, Cu, or Ce via photo deposition. In this study advances our understanding of metal-doped TiO_2 photocatalysts and supports their potential applications in biomaterials.

In previous studies, we leveraged fluorine-doped TiO_2 nanocrystals (F-TiO_2 NS) to demonstrate that highly ordered TiO_2 nanosheets with exposed [001] facets exhibit superior photocatalytic activity to conventional TiO_2 nanoparticles [1]. In the current study, we first prepared F-TiO_2 NS and subsequently washed them with NaOH solution to obtain fluorine-reduced nanosheets, referred to as TiO_2 NS. To further investigate the potential of heterojunction photocatalysts, we doped TiO_2 NS with Ag, Cu, or Ce via photodeposition, successfully synthesizing three metal-doped specimens: Ag/TiO_2 NS, Cu/TiO_2 NS, and Ce/TiO_2 NS [2].

We characterized these materials and evaluated their photocatalytic potential by assessing the generation of reactive oxygen species (ROS) and antibacterial activity against S. mutans. Electron spin resonance (ESR) analysis using 5,5-dimethyl-1-pyrroline-N-oxide (DMPO) confirmed significant ROS generation in Ag/TiO_2 NS and Ce/TiO_2 NS (Fig. 1). In contrast, F-TiO_2 NS and Cu/TiO_2 NS produced lower levels of ROS, although they were still higher than those generated by pure TiO_2 NS, which generated the least amount of ROS.

The antibacterial activity of the specimens (0.10 mg/mL) against *Streptococcus mutans* was evaluated under UV irradiation (Fig. 2). While all the specimens exhibited antibacterial effects over time, Cu/TiO_2 NS achieved nearly 90% bacterial reduction within 1 h of UV irradiation. This was significantly higher than the approximately 50% reduction observed with pure TiO_2 NS, indicating that both surface fluorine and Cu doping enhanced the antibacterial efficiency under UV irradiation.

In summary, ESR analysis confirmed that all doped TiO_2 NS generated greater amounts of ROS than pure TiO_2 NS, suggesting enhanced electron-hole separation.

Notably, the Cu/TiO_2 NS demonstrated markedly improved antibacterial activity. These findings provide deeper insight into the physicochemical and photochemical roles of Ag, Cu, and Ce dopants in modulating surface adsorption and charge dynamics in TiO_2-based materials.

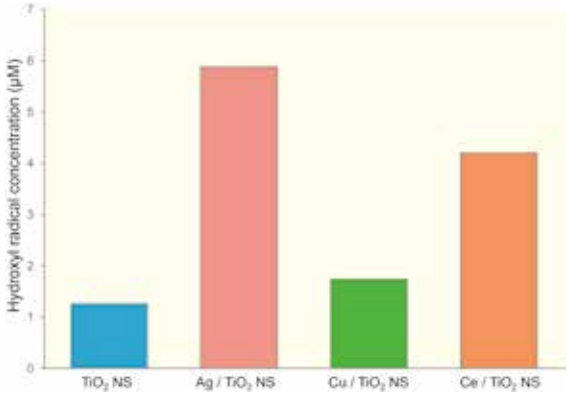

Fig. 1 Concentration of hydroxyl radical generation under UV irradiation

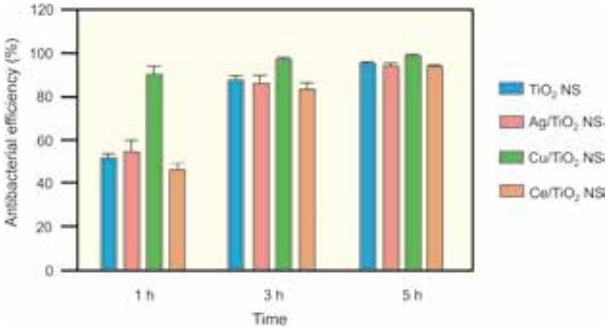

Fig. 2 Antibacterial activity under UV irradiation

References

[1] K. Hayashi, K. Nozaki, Z. Tan, K. Fujita, R. Nemoto, K. Yamashita, H. Miura, K. Itaka, and S. Ohara, Materials **13**, 78 (2020).

[2] M. Jiang, K. Nozaki, T. Mokudai, Y. Nakano, M. Uo, K. Yamashita, S. Ohara, and N. Wakabayashi, ACS Appl. Nano Mater. **8**, 22 (2025).

Takayuki Mokudai (Design & Engineering by Joint Inverse Innovation for Materials Architecture)
E-mail: tmokudai@tohoku.ac.jp
Hidemi Kato (Project Leader of Design & Engineering by Joint Inverse Innovation for Materials Architecture)
E-mail: hidemi.kato.b7@tohoku.ac.jp
URL: http://www.rokken-pjt.imr.tohoku.ac.jp/index.html

Energy-Related Materials

IMR KINKEN Research Highlights 2026

GIMRT

Control of Nucleation and Growth of the Colloidal Crystals by Heteroepitaxy

Heteroepitaxial growth techniques enable controlled nucleation and growth of colloidal crystals. We demonstrate the formation of open structures, including a Kagome lattice, that cannot be achieved by conventional methods. In-situ observations of the crystallization process further provide new insights into the nucleation and growth mechanisms associated with polymorph formation.

Colloidal crystals have attracted significant attention across diverse research fields due to their wide-ranging applications in photonics, sensing, and catalysis. Achieving these functionalities requires precise structural control of the colloidal assemblies. Colloidal epitaxy, in which a template such as a patterned substrate guides crystal growth, is a widely used strategy for this purpose. However, conventional colloidal epitaxy has been largely limited to homoepitaxial growth, where the lattice spacing and symmetry of the substrate closely match those of the growing crystal. Recently, we advanced this technique to realize heteroepitaxy, in which the substrate and the epitaxial phase possess different lattice structures. This approach enables the fabrication of novel architectures that are difficult or impossible to obtain through conventional homoepitaxy. For example, we successfully produced a colloidal kagome lattice (Fig. 1a) [1]. Moreover, heteroepitaxy substantially enhances the nucleation rate, making it particularly suitable for studying systems with slow nucleation kinetics, such as binary colloidal crystals (Fig. 1b) [2].

The increased nucleation rate also allows direct observation of crystallization pathways involving metastable phases. Using this advantage, we established a polymorphic system in single-component colloidal crystals [3]. Unlike the familiar bcc, fcc, or hcp polymorphs of hard-sphere systems, our system exhibits two distinct structures: three-dimensional island-like assemblies (α-phase) and two-dimensional layered structures (β-phase) (Fig. 2). The relative stability of these polymorphs reverses depending on the polymer concentration, which tunes the strength of depletion attraction between particles.

Our study reveals that polymorphic transitions (PTs) between the α- and β-phases occur during nucleation, growth, and dissolution, and can be classified into three types: two solid-state transitions and one solution-mediated transition. The solution-mediated PT is particularly noteworthy, as it is characteristic of attractive colloidal systems and rarely observed in hard-sphere systems. These PTs give rise to nonclassical crystallization pathways in which metastable phases act as intermediates. We demonstrate that the stability of metastable clusters—rather than bulk thermodynamic stability—governs PTs during nucleation, while the size of the polymorph plays a key role during growth. Ultimately, the probabilities of these PTs determine the crystallization pathway and the final crystal structure.

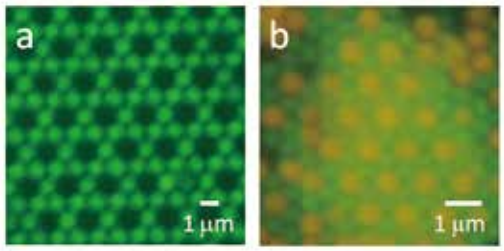

Fig. 1 (a) Open structure colloidal crystals (kagome lattice). (b) Binary colloidal crystals.

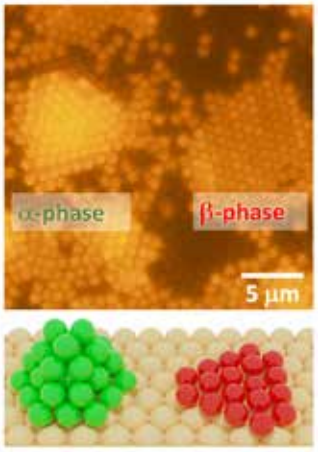

Fig. 2 Two polymorphs of three-dimensional islands (α-phase) and layers (β-phases) formed by heteroepitaxy.

References

[1] J. Nozawa, M. Sato, S. Uda, and K. Fujiwara, Colloid Interface Sci. Commun. **64**, 100815 (2025).

[2] J. Nozawa, M. Sato, S. Uda, L. Chuang, and K. Fujiwara, Cryst. Growth Des. **25**, 7309 (2025).

[3] J. Nozawa, M. Sato, S. Uda, and K. Fujiwara, Commun. Phys. **8**, 134 (2025).

Jun Nozawa (Crystal Physics Research Laboratory)
E-mail: jun.nozawa.e3@tohoku.ac.jp
URL: https://www.xtalphys.imr.tohoku.ac.jp

GIMRT International Co-Authored Paper

Effects of P on Formation and Growth of Mn-Ni-Si Clusters in Low-Cu Reactor Pressure Vessel Steel Analyzed by Atom Probe Tomography

Atom probe tomography was used to analyze effects of P on the formation and growth of Mn-Ni-Si clusters in surveillance test specimens of a low-Cu reactor pressure vessel steel. P-decorated interstitial-type dislocation loops were formed at the initial stage of neutron irradiation, which acted as heterogeneous nucleation sites for a part of the Mn-Ni-Si cluster formation. Consequently, the Mn-Ni-Si clusters were complexes involving dislocation loops.

Reactor pressure vessel (RPV), which is virtually non-replaceable component, limits the achieving safe operation of the reactor because RPV steel is exposed to long-term neutron irradiation field and becomes embrittled. The main origin of the hardening embrittlement is nm-scale Mn-Ni-Si-rich clusters (MNSCs) induced by neutron-irradiation in the case of low-Cu RPV steels. However, the mechanism for MNSC formation is still unclear. The present study [1] demonstrates that P significantly affects the formation and growth of MNSCs in the bulk of low-Cu RPV steels.

The samples employed are surveillance test specimens of a European pressurized water reactor (PWR) having a low Cu content of 0.05 wt.% neutron-irradiated up to the fluence of 1.2×10^{24} n m^{-2}, where n indicates neutrons. Atom probe tomography (APT) was used to investigate the neutron fluence dependence of MNSCs.

Atom maps for P, C, Ni, Mn, Si, Cu and Mo in the unirradiated specimen are presented in Fig. 1(a) along with a transmission electron microscopy (TEM) image of the same needle specimen prior to the APT analyses. Two grain boundaries, labeled “GB” in this figure, are visible in the TEM image and the segregation of various elements at these grain boundaries is evident in the atom maps. It is apparent that elements other than C and Mo were uniformly distributed throughout the grain.

Figure 1(b) shows atom maps in the neutron-irradiated specimens (1.3×10^{23} n m^{-2}). The spatial distribution of P atoms differed between areas with high and low dislocation densities. Specifically, many what appeared to be P clusters were found in the low-density regions during the initial stage of neutron irradiation but such clusters were rare in high-density regions. Although they look like P clusters on the atom map, they are interstitial-type dislocation loops decorated with P.

Figure 2 shows neutron fluence dependence of magnified atom maps of P, Ni, Mn, Si and Cu within the region having a low dislocation line density. In neutron-irradiated specimens from 3.4×10^{23} to 1.2×10^{24} n m^{-2}, Ni, Mn, and Si atoms were enriched at the position of P clusters. No clusters containing solely P were identified. This means that Ni, Mn, and Si atoms aggregate at the position of P clusters and form MNSCs with enrichment of P atoms. P clusters appear to be nucleation sites of MNSCs. This also means the formation of complexes of dislocation loops and MNSCs. The detailed analysis revealed that the presence of P at the clusters enhances the growth of the clusters.

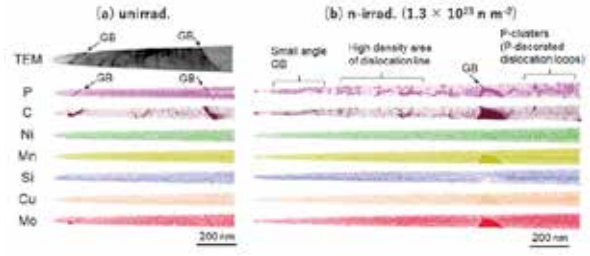

Fig. 1 Atom maps for P, C, Ni, Mn, Si, Cu and Mo in (a) unirradiated and (b) n-irradiated (1.3×10^{23} n m^{-2}) specimens.

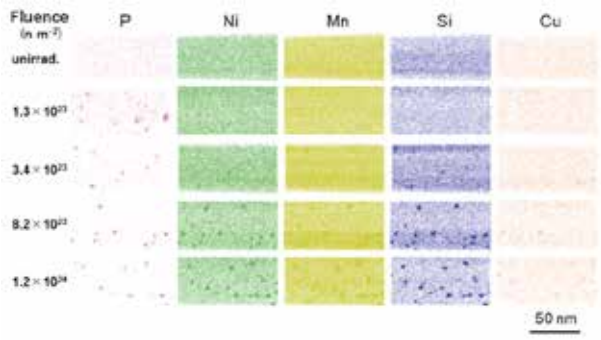

Fig. 2 Neutron fluence dependence of magnified atom maps of P, Ni, Mn, Si and Cu within the region having a low dislocation line density.

References

[1] K. Inoue, C. Zhao, R. Shibahara, K. Kurano, Y. Kume, T. Toyama, M. J. Konstantinović, M. De Smet, R. Gérard, and Y. Nagai, Acta. Mater. **296**, 121303 (2025).

Koji Inoue (Irradiation Effects in Nuclear and Their Related Materials Research Laboratory)
E-mail: koji.inoue.e2@tohoku.ac.jp
URL: https://www.imr.tohoku.ac.jp/en/about/divisions-and-centers/research-division/11.html

International Co-Authored Paper

Suppression of Irradiation Hardening Observed in W-Coated Ferritic Steel for Fusion Reactor Blanket

W-coated reduced activation ferritic steels, such as W/F82H, are candidates for plasma-facing components in fusion reactors due to their sputtering resistance and mechanical strength. This study evaluated neutron irradiation effects on hardness and microstructure in W/F82H. We found that irradiation hardening was suppressed in W, F82H, and the interface in the W/F82H.

Materials resistant to extreme environments, such as oxide dispersion strengthened (ODS) alloys [1,2], ceramics [3,4] and heavy alloys, are crucial for realizing advanced nuclear systems, such as Gen IV fission reactors and fusion reactors. W-coated reduced-activation ferritic steels, such as W/F82H, is a promising candidate for the first wall structural material in fusion reactors. However, effect of neutron irradiation on the mechanical properties in the W-coated reduced-activation ferritic steels is unclear. In this study, we performed neutron irradiation experiments on W/F82H specimens by using BR2, SCK CEN and HFIR, ORNL under their international collaborations [5].

As a result, after neutron irradiations in BR2, irradiation hardening was significantly suppressed across all regions of underwater explosive-welded W/F82H, whereas stand-alone W and F82H exhibit typical hardening under similar irradiation conditions. The W/F82H consisted of four distinct regions: (i) W, (ii) a thin W–F82H mixed interlayer (~10 μm), (iii) an under-coat hardened (UCH) zone extending to ~100–120 μm in F82H, and (iv) the unaffected base F82H. Despite the formation of irradiation defects (black-dot type defects) in W detected by WB-STEM, no net irradiation hardening occurred. Hardness evolution shows that the UCH zone softens under both 290 °C neutron irradiation and equivalent thermal ageing, indicating recovery of work-hardening introduced by explosive welding. In W, the expected irradiation hardening is offset by the same recovery mechanism. In the F82H base metal, irradiation hardening is completely suppressed; This is attributed to residual elastic stress caused by coefficient-of-thermal-expansion mismatch (W < F82H), consistent with literature where elastic tensile stress suppresses formation of irradiation-induced clusters during irradiation. Therefore, this suppression is explained by residual stress from thermal expansion mismatch and the unique microstructure at the interface. These results provide valuable insights for the development of more durable materials in nuclear fusion applications.

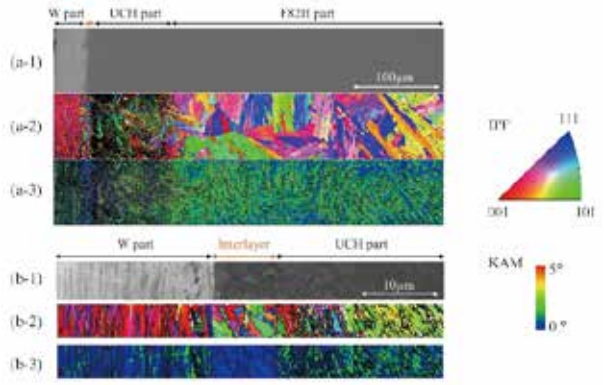

Fig.1 (a,b-1) SEM image, (a,b-2) IPF map, and (a,b-3) KAM map of unirradiated W/F82H: (a) wide area and (b) narrow area.

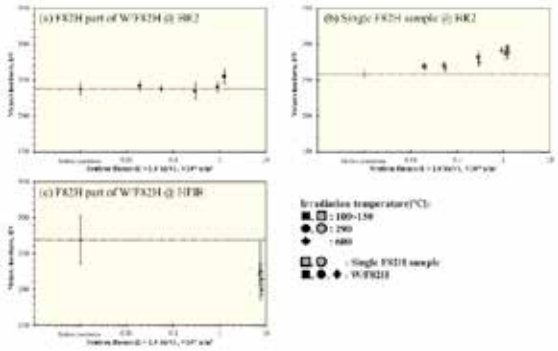

Fig. 2 Comparison of the neutron-dose-dependence of Vickers hardness in the F82H part of irradiated W/F82H and non-welded single F82H.

References

[1] Geng, H. Yu, Y. Ogino, S. Kondo, J. Miyazawa, and R. Kasada, Materials & Design **260**, 115218 (2025).

[2] H. Yu, D. Geng, Y. Ogino, N. Oono-Hori, K. Inoue, S. Kondo, R. Kasada, and S. Ukai, J. Nucl. Mater. **606**, 155663 (2025).

[3] X. Yuan , S. Kondo, D. Geng, K. Yabuuchi, H. Yu, Y. Ogino, and R. Kasada, J. Eur. Ceram. Soc. **45**, 117563 (2025).

[4] T. Miyagishi, S. Kondo, H. Katsui, K. Yabuuchi, R. Usukawa, Y. Ogino, H. Yu, and R. Kasada, J. Nucl. Mater. **603**, 155410 (2025).

[5] K. Seki, K. Yoshida, H. Miyata, A. Hasegawa, S. Kondo, H. Yu, Y. Ogino, K. Hokamoto, S. Tanaka, T. Koyanagi, and R. Kasada, J. Nucl. Mater. **607**, 155657 (2025).

Ryuta Kasada, Sosuke Kondo, Hao Yu, Yasuyuki Ogino, and Minha Park (Nuclear Materials Engineering Research Laboratory)
E-mail: ryuta.kasada.e7@tohoku.ac.jp
URL: https://web.tohoku.ac.jp/imr-numat/

Crystal Structure Determination of the Layered $Cu_{2-\delta}Te$ Low-Temperature Phase by Complementary Use of Scanning Transmission Electron Microscopy and X-Ray Diffraction

Crystal structure of the $Cu_{2-\delta}Te$ room-temperature phase has long been controversial, leading to ambiguous discussions of its thermoelectric properties. We resolve these inconsistencies by combining atomic-resolution scanning transmission electron microscopy (STEM), X-ray diffraction, and first-principles calculations. The complementary use of these techniques reveals a layered structure with a high density of van der Waals-like interlayer Te–Te bonds, providing a reliable structural basis for understanding its low lattice thermal conductivity.

Compounds with the inverse fluorite structure, M_2X (M = Cu, Ag; X = S, Se, Te), are known to exhibit extremely low lattice thermal conductivity at high temperatures owing to a high concentration of M-site vacancies and the high mobility of M atoms with high Seebeck coefficient and electrical conductivity. Therefore, some of them are promising candidates for thermoelectric materials. Upon cooling, partial ordering of atoms and vacancies leads to the emergence of multiple compound phases. In the Cu–Te system, a large number of low-temperature phases and reaction pathways have been reported, and numerous crystal structure models have been proposed. Nevertheless, inconsistencies in reported crystal symmetries and atomic arrangements persist, and thermoelectric properties have often been discussed without reliable phase identification.

A fundamental difficulty arises from the limitations of conventional structural analysis techniques. X-ray diffraction (XRD) provides three-dimensional crystallographic information, but only as an average over a wide sample volume. Structural models must therefore be obtained through inverse analysis of diffraction intensities, which frequently yields incorrect solutions for complex, non-stoichiometric, or long-period structures. In contrast, scanning transmission electron microscopy (STEM) enables direct real-space observation of atomic arrangements with high spatial resolution, allowing highly reliable identification of local structural motifs. However, STEM inherently provides two-dimensional projection images, and accurate determination of three-dimensional atomic positions remains challenging.

In this work, we demonstrate that the crystal structure of the $Cu_{2-\delta}Te$ room-temperature phase can be reliably established only by combining these complementary techniques, further supported by first-principles calculations [1]. By performing systematic electron diffraction, atomic-resolution STEM, SEM/EDS, and powder XRD analyses, we show that the $Cu_{2-\delta}Te$ room-temperature phase is a line compound slightly shifted toward the Te-rich side. Electron diffraction extinction rules indicate rhombohedral symmetry, while in-plane STEM observations reveal a layered structure composed of six-layer slabs,

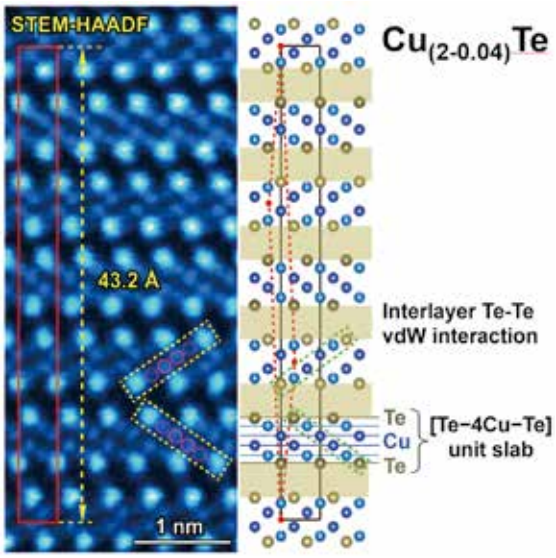

Fig. 1 STEM-HAADF image of $Cu_{1.96}Te$ taken along an in-plane direction. The darker contrast of Cu atoms in the outer layers is due to the Cu vacancy as well as its large atomic displacement. No atom exists in the Te–Te interlayer bonds.

[Te–Cu–Cu–Cu–Cu–Te]. The non-stoichiometry originates from approximately 4% structural vacancies on outer-layer Cu sites, yielding a composition close to $Cu_{1.96}Te$ [1].

Adjacent slabs are connected by Te–Te bonds that exhibit van der Waals-like character. Remarkably, despite the relatively low Te content (~34 at.%), the density of these interlayer Te–Te bonds is comparable to that in Bi_2Te_3 (60 at.%). The exceptionally low lattice thermal conductivity of this phase is therefore attributed to the combined effects of Cu-site vacancies and the anharmonicity associated with van der Waals-like Te–Te bonding [1]. The present study highlights the necessity of combining XRD, STEM, and first-principles calculations to avoid erroneous structural models and to establish a reliable structure–property relationship in complex thermoelectric materials.

References

[1] Y. Zhang, N. L. Okamoto, and T. Ichitsubo, Chem. Mater. **37**, 5365 (2025).

Norihiko L. Okamoto and Tetsu Ichitsubo (Structure-Controlled Functional Materials Research Laboratory)
E-mail: nlokamoto@tohoku.ac.jp, tichi@tohoku.ac.jp
URL: http://ilab.imr.tohoku.ac.jp/

GIMRT

Crystal Structure Investigations of $LaNi_2$ and its Hydride with Trigonal Prisms Synthesized by a High-Pressure Technique

New hydride ($LaNi_2H_3$) was synthesized at 6 GPa by a high-pressure technique. Using synchrotron radiation, and neutron diffraction, $LaNi_2H_3$ was elucidated to form through a new intermetallic compound $LaNi_2$. Both crystal structures were composed of trigonal prisms with La and Ni atoms. In addition, hydrogen atoms in $LaNi_2H_3$ were located around Ni atom at a distance of 1.40 Å.

Intermetallic compounds react with hydrogen gas under hydrogen gas pressure and store (absorb) hydrogen atoms in interstitial sites in metal atom arrangements. The hydrogen absorption reaction corresponds to formation of hydride phases, in which the absorbed hydrogen atoms are released under decreasing hydrogen gas pressure. Therefore, such intermetallic compounds are expected to be promising hydrogen storage materials. In general, the hydrogen absorption and desorption reactions are measured below 10 MPa. By contrast, the hydrogen absorption reactions are dramatically promoted above 1 GPa. This indicates that high-pressure experiments above 1 GPa can be employed for investigations of maximum hydrogen storage capacities and exploration of new hydride phases.

Recently, we reported that a typical hydrogen storage material $LaNi_5$ absorbed hydrogen up to 2.1 mass% at 10 GPa (Fig. 1) [1]. The hydrogen storage capacity at 10 GPa was 1.5 times higher than that of $LaNi_5$. In addition, a new La-Ni hydride phase was also identified after hydrogen absorption reactions on $LaNi_5$.

To elucidate the new La-Ni hydride phase, we synthesized isotopically labeled La-Ni deuteride, of which crystal structure was elucidated by synchrotron radiation X-ray and neutron diffraction. Resulting that, new La-Ni deuteride could be identified as $LaNi_2D_3$, which was formed through a new intermetallic compound $LaNi_2$ with Fe_2P-type structure [2].

Figure 2 shows crystal structures of $LaNi_2$ and $LaNi_2D_3$ [2]. In $LaNi_2$, La and Ni atoms were arranged in a distorted trigonal prism. The distorted trigonal prism in $LaNi_2$ became an undistorted trigonal prism in $LaNi_2D_3$ due to the insertion of deuterium (hydrogen) atoms above 500 °C and 6 GPa. In the crystal structure of $LaNi_2D_3$, some of the deuterium atoms were located around Ni atoms at a distance of 1.40 Å, which is similar to Ni–D distances and atomic arrangements in intermediate NiD_{2-3} units for $[NiD_4]^{4-}$ in a complex hydride $LaMg_2NiD_7$ with higher hydrogen storage capacities [3].

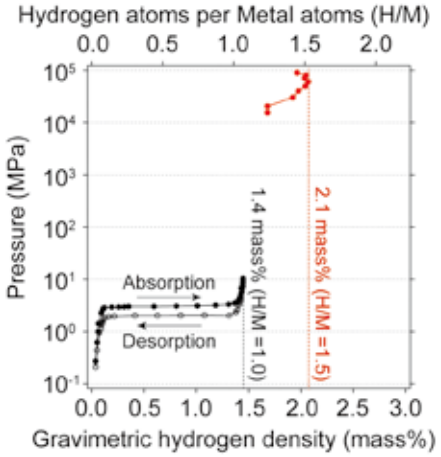

Fig. 1 Hydrogen absorption reactions on $LaNi_5$. The reactions were observed by Pressure-Composition-Temperature (PCT) apparatus at 30 °C below 1 MPa (black) and at room temperature above 1 GPa (red).

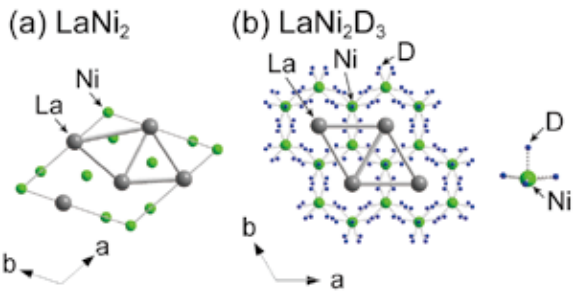

Fig. 2 Crystal structures of (a) $LaNi_2$, and (b) $LaNi_2D_3$. In $LaNi_2D_3$, D atoms around Ni atom with interatomic distances of Ni-D: 1.4 Å shows in the right. In the crystal structures, La, Ni and D atoms show gray, green, and blue spheres, respectively. The trigonal prism shows think gray lines in $LaNi_2$ and $LaNi_2D_3$.

References

[1] T. Sato, H. Saitoh, R. Utsumi, J. Ito, Y. Nakahira, K. Obana, S. Takagi, and S. Orimo, Molecules **28**, 1256 (2023).

[2] T. Sato, R. Utsumi, Y. Nakahira, H. Saitoh, T. Honda, and S. Orimo, Inorg. Chem. **64**, 21534 (2025).

[3] K. Miwa, T. Sato, M. Matsuo, K. Ikeda, T. Otomo, S. Deledda, B.C. Hauback, G. Li, S. Takagi, and S. Orimo, J. Phys. Chem. C **120**, 5926 (2016).

Toyoto Sato and Shin-ichi Orimo (Hydrogen Functional Materials Research Laboratory)
E-mail: toyoto.sato.d4@tohoku.ac.jp
URL: https://www.hydrogen.imr.tohoku.ac.jp/en/index.html

International Co-Authored Paper

Fundamental Design Guidelines and Evaluation Protocols for Advanced Light-Rechargeable Photobattery Development

Photobatteries, which integrate light-energy harvesting and storage units within a single device, are attracting significant interest driven by the increasing demand for autonomous IoT devices. We recently provided a perspective on this emerging technology, establishing fundamental design guidelines and protocols necessary for the rational development of light-rechargeability in these devices.

Light-rechargeable photobattery devices offer potential advantages in compactness and cost-effectiveness over the conventional systems that combine separate solar cells and batteries. In such conventional systems, four electrodes (i.e., two per device) are typically required, whereas photobatteries share one or more electrodes, reducing the total number to three or even two (Fig. 1). Although the basic concept was reported several decades ago, the development of practical photobatteries has been hindered by technical challenges as well as misconceptions. To address these issues, we recently provided a critical perspective [1], including comprehensive discussions of (i) energetic criteria for electrode materials, (ii) methods to distinguish between the optical and thermal effects, and (iii) proper testing protocols depending on the type of light–battery interactions.

Careful consideration of band alignment plays a central role in the design of photobatteries. For example, while anatase TiO_2 is often used as a photoelectrode material, the energy level of its conduction band minimum is not sufficiently high to reduce (i.e., charge) commonly used metal anode materials such as Li, Na, and even Zn. A way to overcome this is to use a higher-potential anode material (e.g., $Li_2Mn_2O_4$, Cu) to meet the energetic criteria. Another option is to employ tandem or module-type solar cells to boost the photovoltage within the device, which is currently under investigation.

In photoelectrochemical measurements, both the optical and thermal effects are usually tangled and contribute to the photobattery performance. We therefore established a method to distinguish them by plotting the charging rate against the light intensity [2]. The optical contribution exhibits a linear dependence on light intensity, while the thermal contribution follows an Arrhenius-type exponential dependence. A case study was conducted using TiO_2-based electrodes with varying bias voltages to control the photocharging mode. The results clearly demonstrated a threshold voltage, where the main contribution shifted from thermal to optical effects, providing strong proof of the feasibility of our method.

Finally, to demonstrate photocharging driven by the photovoltaic contribution, we recommended employing chronoamperometry rather than the conventional constant-current measurements. As detailed in our paper [1], it is a rational approach to first build a photo-assisted system with a half-cell design and then construct a fully photo-rechargeable device. We hope our fundamental work lays the foundation for novel photobattery development and contributes to establishing a future sustainable society.

References

[1] A. Pujari, K. Shimokawa, and M. De Volder, Joule **9**, 101869 (2025).

[2] L. Tan, B.-M. Kim, K. Shimokawa, S. J. Heo, A. Pujari, and M. De Volder, ACS Electrochem. **1**, 921 (2025).

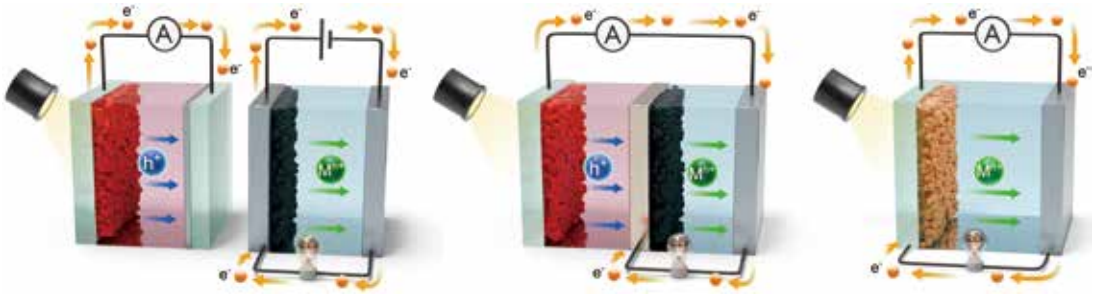

Fig. 1 Schematic illustration showing the fundamental structures for the separated system (left), as well as the integrated three-electrode (middle) and two-electrode (right) photobatteries [1].

Kohei Shimokawa (Exploratory Research Laboratory)
E-mail: kohei.shimokawa.b7@tohoku.ac.jp
URL: https://www.imr.tohoku.ac.jp/en/about/divisions-and-centers/research-division/33.html

Electronic Materials

IMR KINKEN Research Highlights 2026

Electron Correlations in Nickelate Superconductors

Superconductors are an important research topic in materials science because of their potential applications. Among them, unconventional superconductors have attracted considerable attention because they can exhibit high superconducting transition temperatures; however, the mechanism of superconductivity in these materials remains unresolved. In this study, we theoretically investigate the electronic structure of newly discovered nickelate unconventional superconductors, with a particular focus on electron correlations, in order to deepen the understanding of their superconducting properties.

The quest to understand high-transition-temperature (T_c) superconductivity (SC) remains a central issue in condensed matter physics. In this context, the recent discovery of SC in nickelates has generated significant interest.

There are two classes of nickelate superconductors. One is infinite-layer nickelates, whose electronic structure is expected to be similar to that of the celebrated high-T_c cuprates. In Ref. [1], we investigate the electronic structure, in particular electron correlation effects, in an infinite-layer nickelate (La,Sr)NiO_2 by comparing theoretical and experimental results for transport properties (Hall and Seebeck coefficients). (La,Sr)NiO_2 shows a T_c dome as a function of Sr doping, and we have found that whereas the correlation effects in the large-doping region can be well described by elementary correlation effects (quasiparticle mass enhancement and temperature dependence of scattering rate), those in the small-doping region cannot. This suggests that there exist nontrivial correlation effects in the small-doping region that may give rise to an exotic state of matter such as a pseudogap state. This puts infinite-layer nickelates in the category of strongly correlated superconductors, as in the case of cuprates.

We also investigate the electron correlation effects and pairing mechanism in the other class of nickelates superconductors; bilayer nickelate $La_3Ni_2O_7$ (for experimental progress on thin-film bilayer nickelates, see Ref. [2]). As a canonical model hosting high-T_c SC and as an effective model for $La_3Ni_2O_7$, we investigate the bilayer Hubbard model on a square lattice [3] using state-of-the-art cluster dynamical mean-field theory. Unlike the d-wave SC observed in doped Mott insulators such as cuprates, the bilayer model exhibits $s_\pm$-wave SC emerging from a correlated band insulator, where dynamical band repulsion drives the insulating behavior [3]. We uncover kinetic-energy-driven [BEC(Bose-Einstein condensation)-like] SC in a small-doping region and its crossover to conventional potential-energy-driven [BCS(Bardeen Cooper Schrieffer)-like] SC. Above T_c, we observe an unusual metallic state with a striking momentum-space dichotomy in the kinetic-energy-driven regime: one Fermi pocket develops a pseudogap while the other becomes nearly incipient.

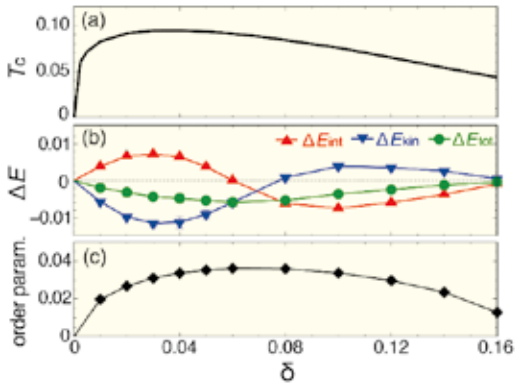

Fig. 1 (a) Doping dependence of T_c of $s_\pm$-wave SC in the bilayer Hubbard model. The maximum T_c reaches as high as 10% of the in-plane hopping. (b) Energy difference between SC and normal states. We see a crossover from the kinetic-energy-driven (BEC-like) regime to the conventional potential-energy-driven (BCS-like) regime with increasing doping δ. (c) Order parameter of $s_\pm$-wave SC. The dome-shaped behavior of the order parameter as a function of doping also indicates a BEC–BCS crossover.

Despite differences in pairing symmetry and parent insulating states, we identify strong momentum-space dichotomy as a remarkable commonality between d-wave SC (antinodal vs. nodal regions) and $s_\pm$-wave SC (electron vs. hole pockets).

Using a novel method for estimating the coherence length in strongly correlated SC, we reveal that the coherence length of the $s_\pm$-wave SC is only a few lattice constants, corresponding to approximately 1 nm in $La_3Ni_2O_7$, which accounts for the exceptionally high critical field (~ 100 T) observed experimentally.

References

[1] M. Osada, S. Imajo, Y. Seki, K. Ishida, T. Nojima, K. Fujiwara, K. Kindo, Y. Nomura, and A. Tsukazaki, Sci. Adv. **11**, eadv6488 (2025).
[2] M. Osada, C. Terakura, A. Kikkawa, M. Nakajima, H.-Y. Chen, Y. Nomura, Y. Tokura, and A. Tsukazaki, Commun. Phys. **8**, 251 (2025).
[3] Y. Nomura, M. Kitatani, S. Sakai, and R. Arita, Phys. Rev. B **112**, L020504 (2025).

Yusuke Nomura (Theory of Solid State Physics Research Laboratory)
E-mail: yusuke.nomura@tohoku.ac.jp
URL: https://www.nomura-lab.imr.tohoku.ac.jp

GIMRT International Co-Authored Paper

Observation of the Low Energy Mode Anomaly at Magnonic Dicke Superradiant Phase Transition

Anomalous softening of low energy magnon mode in $ErFeO_3$ has been observed by the semicontinuous transmission ESR spectroscopy by combining tunable THz monochromatic sources and pulsed magnetic fields. The softening of the magnon is clearly identified at the magnonic Dicke superradiant phase transition. The transition field coincides with the kink of the quasi-antiferromagnetic mode observed by the THz time domain spectroscopy.

A coherence can be produced among two-level atoms by cooperative interaction with a single-mode quantized radiation field. A realization of such state and applicability of Dicke model have been extensively studied for decades. One of the most important outcomes of the Dicke model is a quantum phase transition, called super-radiant phase transition, where a static coherent electric or magnetic field and a finite atomic polarization appear spontaneously and cooperatively. Realization of the super-radiant state has been examined extensively, but no-go theorem seems to prevent the occurrence such state in thermal equilibrium.

A new route for the super-radiant phase transition has been proposed by theoretical study. It suggested that a magnetic analog of the transition can occur for the absence of the A^2 term. The target material is the $ErFeO_3$ where two types of magnetic ions, Er and Fe are involved. The scenario of the phase transition is that magnons of the Er and Fe sublattices are coupled strongly and the coupling induces the cooperative and coherent state. An interesting point in the magnetic analog is that the magnon-magnon coupling can be tuned by an external magnetic field.

In $ErFeO_3$, there are two magnon modes, one is the high energy magnon related to the Fe sublattice and the other is the low energy magnon of the Er sublattice. The field dependence of these magnon modes have been examined by three methods, THz-time domain spectroscopy in a pulsed magnetic field, a calorimetric detection THz spectroscopy and a semicontinuous ESR transmission spectroscopy in a pulsed magnetic field.

Figure 1 shows the ESR spectrum between 33 and 109 GHz. The softening of the mode around the critical field of 1. 7 T is clearly identified. The anomaly of the high energy magnon is found as the kink of the mode at the same magnetic field. The coincidence of anomaly shows the strong and magnetic field tunable magnon-magnon coupling in $ErFeO_3$.

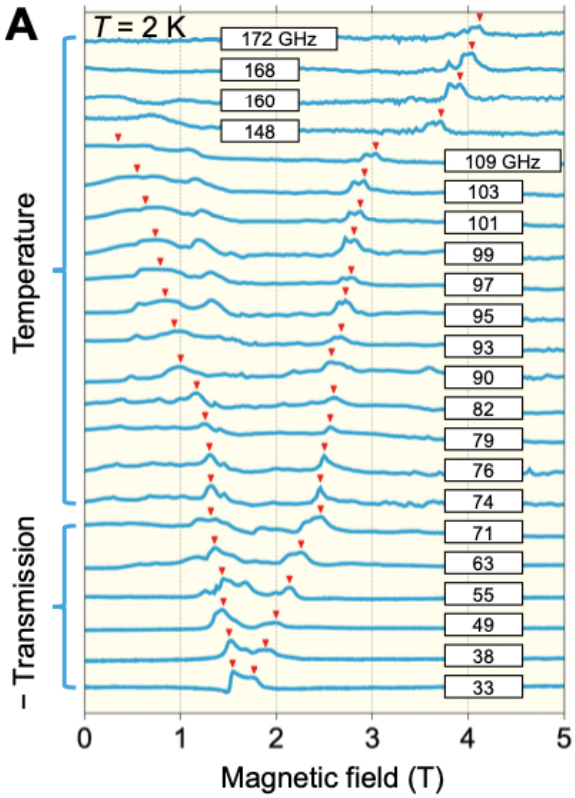

Fig. 1 Transmission ESR spectroscopy for low energy magnon mode [1].

The present investigation shows the potential of hetero-magnetic materials as the model system for cavity QED research and the importance of THz spectroscopy and THz ESR in high magnetic fields for such investigations.

References

[1] D. Kim *et al*, Science Advances **11**, eadt1691 (2025).

Hiroyuki Nojiri (Magnetism Research Laboratory)
E-mail: hiroyuki.nojiri.e8@tohoku.ac.jp
URL: https://www.hfpm.imr.tohoku.ac.jp

GIMRT

Infrared Magneto-Optical Spectroscopy Unveils Altermagnetism in an Organic "Antiferromagnet"

We developed a novel infrared magneto-optical approach for anisotropic crystals to identify altermagnetism, a recently proposed magnetic state combining characters of both ferro- and antiferromagnets. Using the organic antiferromagnet κ-(BEDT-TTF)$_2$Cu[N(CN)$_2$]Cl, we experimentally revealed off-diagonal conductivity spectra containing altermagnetic and non-altermagnetic components, reflecting intertwined spin, charge, and lattice contributions.

Magnetism has traditionally been classified into two types: ferromagnetism, where magnetic moments align to produce strong magnetization, and antiferromagnetism, where moments cancel each other. Recently, a third category—altermagnetism—has emerged as a frontier topic in condensed matter physics. Altermagnets exhibit zero net magnetization like antiferromagnets but display ferromagnet-like phenomena such as spin-current generation and anomalous Hall effect. Importantly, the piezomagnetic effect, long considered unique to antiferromagnets, is now understood as a defining property of altermagnets. In fact, the occurrence of piezomagnetism and altermagnetism are nearly synonymous, both originating from the same symmetry-breaking spin arrangement characterized by a magnetic octupole order parameter.

The organic salt κ-(BEDT-TTF)$_2$Cu[N(CN)$_2$]Cl (κ-Cl) was theoretically predicted to host altermagnetism [1, 2]. Its quasi-two-dimensional lattice and strong electron correlations make it an ideal candidate. However, κ-Cl is an electrical insulator, and its fragile crystals preclude conventional probes such as transport measurements, stress application, or X-ray techniques. To overcome these limitations, we employed infrared magneto-optical Kerr effect (MOKE) spectroscopy at SPring-8 BL43IR [3]. A major challenge was the absence of a method to extract off-diagonal optical conductivity, a critical probe for detecting altermagnetism, from anisotropic crystals. Although off-diagonal conductivity can also arise from conventional magneto-optical effects or strain, our analysis based on magnetic-field parity and xy/yx symmetry successfully isolates the altermagnetic component. This capability represents a key advance.

Experiments at 15 K under ±9 T revealed distinct off-diagonal spectral features, including edge peaks absent in diagonal conductivities and mid-energy regions where off-diagonal conductivity scales with diagonal terms. These behaviors indicate three contributions: spin-band splitting associated with altermagnetism, lattice distortion linked to the inverse piezomagnetic effect, and conventional magneto-optical response. By disentangling these components, our method provides direct experimental evidence of altermagnetism in κ-Cl. Beyond this material, the approach offers a powerful tool for exploring chiral and anisotropic systems where off-diagonal optical responses are key.

References

[1] M. Naka, S. Hayami, H. Kusunose, Y. Yanagi, Y. Motome, and H. Seo, Nat. Commun. **10**, 4305 (2019).

[2] M. Naka, S. Hayami, H. Kusunose, Y. Yanagi, Y. Motome, and H. Seo, Phys. Rev. B **102**, 075112 (2020).

[3] S. Iguchi, H. Kobayashi, Y. Ikemoto, T. Furukawa, H. Itoh, S. Iwai, T. Moriwaki, and T. Sasaki, Phys. Rev. Res. **7**, 033026 (2025).

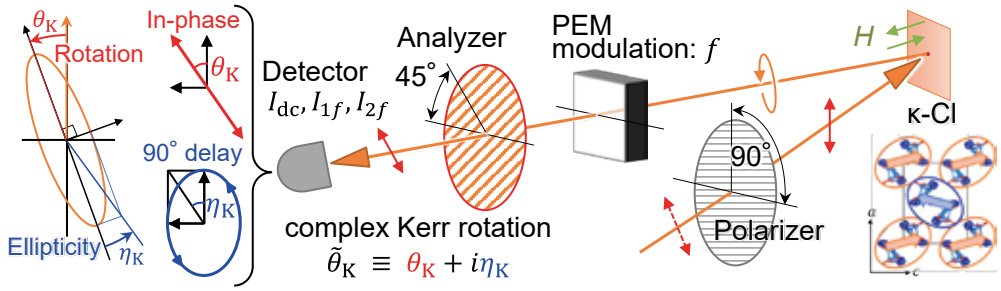

Fig. 1 Schematic of infrared magneto-optical Kerr effect measurement and complex Kerr rotation.

Satoshi Iguchi (Low Temperature Condensed State Physics Research Laboratory)
E-mail: satoshi.iguchi.c8@tohoku.ac.jp
URL: https://cond-phys.imr.tohoku.ac.jp/index_e.html

GIMRT

Study on the Utilization of a ^{3}He Spin Filter Based on Spin-Exchange Optical Pumping at J-PARC

The use of ^{3}He spin filters has been actively pursued for spin-dependent studies with polarized neutrons at the Materials and Life Science Experimental Facility (MLF) of Japan Proton Accelerator Research Complex (J-PARC). A dedicated group at the J-PARC Center conducts approximately ten user experiments annually, covering a broad range of research fields from condensed matter physics to particle and nuclear physics. This report focuses on the development and operation of a compact ^{3}He spin filter that can be deployed within the limited installation space available at neutron beamlines, and summarizes recent efforts toward its practical use.

Polarized neutron beams are widely used in spin-dependent studies in condensed matter, particle, and nuclear physics. The ^{3}He spin filters provide efficient neutron polarization over a broad energy range from meV to eV by exploiting the strong spin dependence of neutron absorption in ^{3}He, whereby neutrons with antiparallel spin are absorbed while those with parallel spin are transmitted. Polarized ^{3}He gas is produced using the spin-exchange optical pumping (SEOP) technique, in which optically pumped rubidium atoms transfer angular momentum to ^{3}He nuclei through spin-exchange collisions.

A key technical challenge in the operation of ^{3}He spin filters is the vulnerability of the ^{3}He polarization to magnetic field inhomogeneities, particularly transverse field components perpendicular to the polarization axis. This issue becomes especially critical in neutron beamline environments at MLF, where iron-based shielding materials are commonly employed. Accordingly, careful optimization of the static magnetic field configuration is required to ensure stable polarization under such conditions. Once polarized, ^{3}He gas can retain its polarization for timescales ranging from several tens to several hundreds of hours, even after the SEOP process has been halted. This long relaxation time enables two distinct operational modes: ex-situ operation, in which SEOP is performed outside the beamline prior to installation, and in-situ operation, in which SEOP is continuously maintained at the beamline during neutron measurements. Spectrometer rooms at MLF are typically populated with instrument-specific equipment optimized for dedicated scientific objectives, leaving only limited space for auxiliary devices such as ^{3}He spin filters. The available installation volume is often restricted to dimensions on the order of several tens of centimeters. For this reason, ex-situ spin filters, which require minimal on-site infrastructure, have historically been favored [1].

Fig. 1 Compact in-situ ^{3}He spin filters.

However, the gradual decay of ^{3}He polarization in ex-situ operation poses a limitation for experiments demanding high polarization stability and precision. To address this issue, compact in-situ ^{3}He spin filters have been developed by optimizing the designs of both the static magnetic field coils and the laser optical system, enabling installation within an approximately 30 cm scale volume [2]. Neutron beam tests of the compact in-situ system were carried out last year, demonstrating a ^{3}He polarization exceeding 70% with continuous operation times longer than 100 hours. Over the past two years, the system has already been successfully employed in several physics experiments. This performance and operational experience suggest that the compact in-situ ^{3}He spin filters represent a promising option for future polarized neutron experiments.

References

[1] T. Okudaira et. al., Nucl. Instrum. Methods Phys. Res. A **977**, 164301 (2020).

[2] S. Takahashi et. al., Nucl. Instrum. Methods Phys. Res. A **1075**, 170410 (2025).

Masaki Fujita (Quantum Beam Materials Physics Research Laboratory)
E-mail: fujita@tohoku.ac.jp
URL: https://qblab.imr.tohoku.ac.jp/ index-e.html

GIMRT International Co-Authored Paper

Nonreciprocal Electronic Transport in Helimagnets

Nonreciprocal electronic transport is electric current rectification induced by the breaking of time reversal and spatial inversion symmetry. It is quite useful, especially for helimagnets, because it can probe the handedness of magnetic structure denoted as chirality. Here, we have investigated the mechanism of nonreciprocal electronic transport in helimagnets EuP_3 and YMn_6Sn_6.

Helimagnet is a kind of antiferromagnet in which the magnetic moments are within a plane perpendicular to the propagation vector, and the in-plane angle gradually increases along the propagation vector to construct a spiral. Two rotational directions of the magnetic spiral (chirality) are transformed into each other by spatial inversion. Recent experiments showed that chirality can be detected by nonreciprocal electronic transport.

There are three possible mechanisms of nonreciprocal transport in a helimagnet, the electronic band asymmetry, the current-induced deformation of the helimagnetic structure, and the asymmetric scattering. To study which mechanism is realized in helimagnets EuP_3 and YMn_6Sn_6, we have investigated the magnetic field and temperature dependence of nonreciprocal electronic transport for these helimagnets [1, 2].

We have fabricated microscale Hall-bar-like devices to apply large electronic current density as shown in Fig. 1 and measured nonreciprocal electronic transport as functions of temperature and magnetic field. In the case of EuP_3, the magnetic field dependence coincided with that calculated based on the band asymmetry mechanism [1]. On the other hand, the nonreciprocal electronic transport shows an enhancement at the phase boundary for YMn_6Sn_6, which is consistent with the asymmetric scattering mechanism (Fig. 2) [2].

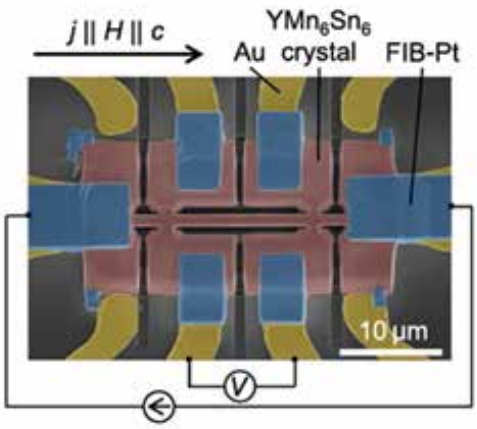

Fig. 1 Scanning electron microscope image of the focused ion beam (FIB) microfabricated YMn_6Sn_6 device [2].

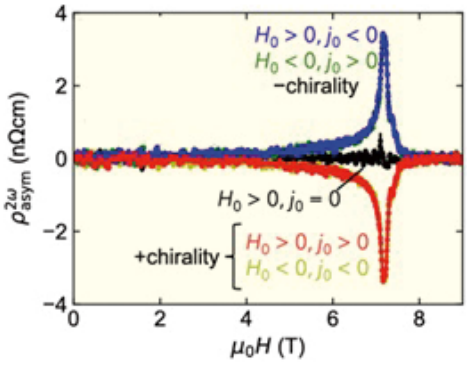

Fig. 2 Magnetic field dependence of nonreciprocal resistivity at 200K for YMn_6Sn_6 [2].

References

[1] A. H. Mayo, D.-A. Deaconu, H. Masuda, Y. Nii, H. Takahashi, R. V. Belosludov, S. Ishiwata, M. S. Bahramy, and Y. Onose, Proc. Natl. Acad. Sci. U.S.A. **122**, e2405839122 (2025).

[2] H. Masuda, J. Ohe, Y. Nii, S. Kimura, and Y. Onose, Phys. Rev. Research **7**, 033019 (2025).

Yoshinori Onose (Quantum Functional Materials Physics Research Laboratory)
E-mail: yoshinori.onose.b4@tohoku.ac.jp
URL: https://onoselab.imr.tohoku.ac.jp/index.html

Growth of Oxide Single Crystals with High Melting Point Using Tungsten Crucible and Deoxygenated Insulator

New crystal growth method using tungsten (W) crucible was developed for crystal growth of oxide single crystals with high melting point (m.p.) above 2200°C. The deoxygenated insulator allows the use of a W crucible without oxidation during crystal growth, and enabling the production of high-quality single crystals without impurities. The advanced crystal growth method enabled the growth of various oxide single crystals such as Lu_3TaO_7, $La_2Hf_2O_7$ and RE_2O_3 with the m.p. above 2200°C.

Most single crystals of oxide materials have been grown by the melt-growth methods using a crucible. In general, precious metal crucibles such as platinum (Pt) and iridium (Ir) crucibles have been used to grow single crystals of oxide materials with relatively high melting points (m.p.) because of their stability against temperature and atmosphere.

However, recent rise in precious metal prices has hindered material research and mass production of functional oxide single crystals. In addition, Ir crucible can only be used in the temperature range below 2200°C, and material research in the temperature range above 2200°C has made little progress.

Therefore, we developed a new crystal growth method that enables the crystal growth of oxide materials with high m.p. above 2200°C (Fig.1) [1]. In the study, we focused on tungsten (W) with higher m.p. than Ir. However, the W is easily oxidized during crystal growth at high temperature, making it impossible to use it as a reaction- and impurity-free crucible.

In consideration of the problems with the W crucible, we developed a deoxygenated insulator to prevent the W crucible from oxidizing due to oxygen released from the insulator during crystal growth. In the deoxygenated process, the conventional ZrO_2 insulator was sintered at 2000°C in Ar using a carbon furnace, and obtained deoxygenated insulator did not release oxygen even at high temperature. As a result, single crystals containing no W particles could be grown from the melt using the W crucible.

First, $La_2Zr_2O_7$ (LZO) single crystal with the m.p. above 2200°C was grown using the advanced crystal growth method [1]. The grown single crystal was black due to oxygen vacancies generated during crystal growth under reducing atmosphere. After annealing in air, the crystal became colorless and transparent. Furthermore, $La_2Hf_2O_7$ (LHO) single crystal with the m.p. above 2400°C could be grown under the same growth conditions. We are the first in the world to successfully grow Lu_3TaO_7 (LTO) single crystal using the method and have applied for a patent.

RE_2O_3 (*RE*: Rare-earth) series are also one of the materials with the m.p. above 2200°C, and their single crystals have not been extensively studied. Therefore, we used the advanced growth method to grow the RE_2O_3 single crystals and realized material exploration. In addition, solid-solution $(RE,RE')_2O_3$ single crystals including two or more *RE* elements have also been grown by the advanced growth method, and Pr- and Tb-doped $(Lu,Y,Sc)_2O_3$ and Eu-doped $(Lu,Y,Sc)_2O_3$ single crystals have been developed for optical thermometry [2, 3] (Fig.2). The advanced growth method is expected to lead to developments of high m.p. oxide single crystals with a variety of advanced functions.

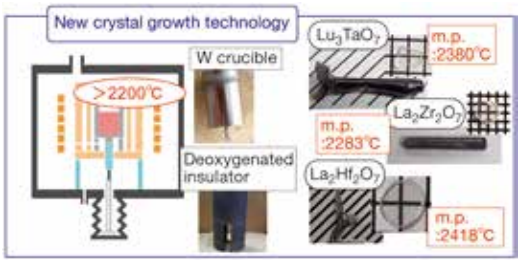

Fig. 1 shows schematic diagram of new crystal growth method and oxide single crystals with high m.p. over 2200°C.

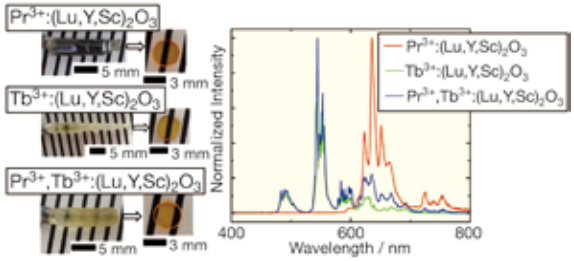

Fig. 2 shows Pr- and Tb-doped $(Lu,Y,Sc)_2O_3$ single crystals and their photoluminescence spectra.

References

[1] Y. Yokota, T. Suda, T. Horiai, and A. Yoshikawa, Sci. Rep. **15**, 27800 (2025).

[2] Y. Abe, T. Horiai, Y. Yokota, M. Yoshino, R. Murakami, T. Hanada, A. Yamaji, H. Sato, Y. Ohashi, S. Kurosawa, K. Kamada, and A. Yoshikawa, J. Mater. Chem. C **13**(16), 8032 (2025)

[3] Y. Abe, T. Horiai, Y. Yokota, M. Yoshino, J. Pejchal, R. Kucerkova, R. Murakami, T. Hanada, A. Yamaji, H. Sato, Y. Ohashi, S. Kurosawa, K. Kamada, M. Nikl, and A. Yoshikawa, J. Lumin. **280**, 121118 (2025)

Yuui Yokota (Advanced Crystal Engineering Research Laboratory)
E-mail: yui.yokota.a5@tohoku.ac.jp
URL: http://yoshikawa-lab.imr.tohoku.ac.jp/

GIMRT International Co-Authored Paper

Guest-Induced Reversible Phase Conversion via Spin Frustration Relief in Spin-Intercalated Layered Antiferromagnets

A spin-intercalated layered MOF magnet is presented, in which paramagnetic metallocenium spins are embedded within an antiferromagnetic host lattice. Competition between interlayer and host–guest exchange interactions generates spin frustration, enabling reversible switching between evident and hidden frustration regimes through solvation control, and resulting in tunable magnetic phase transitions without altering intrinsic spin states.

By methodically altering each building block within molecular assembled architectures and evaluating the predicted magnetic properties, we can deepen our understanding of magnetic materials crafted from molecular building blocks. Leveraging the principles of supramolecular and coordination chemistry, along with Coulomb assembly, has enabled the successful rational assembly of spins into multidimensional molecular frameworks [1-4].

We reported a spin-intercalated layered metal-organic framework (MOF) magnetic system, $[MCp^*_2][\{Ru_2(2,3,5\text{-}F_3ArCO_2)_4\}_2(TCNQ)]\cdot solv$ (M = Co, Fe; $[MCp^*_2]^+$ = decamethylmetallocenium; $2,3,5\text{-}F_3ArCO_2^-$ = 2,3,5-trifluorobenzoate; solv = crystallization solvent), which facilitated reversible magnetic phase switching through the control of spin frustration [5]. In this system, paramagnetic spins ($[FeCp^*_2]^+$ with S = 1/2) are intercalated into a strongly correlated layered antiferromagnet, creating a competition between the interlayer antiferromagnetic coupling ($J_{LL} < 0$) and another coupling between the host and intercalated spins (J_{LS}). The interplay between these interactions dictates the emergence and nature of spin frustration. When $|J_{LS}| \leq |J_{LL}|$, the spin frustration is "evident," leading to a magnetic order accompanied by spin reorientation. Conversely, when $|J_{LS}| >> |J_{LL}|$, the frustration becomes "hidden," and the system displays apparent ferromagnetic or ferrimagnetic behavior despite underlying interlayer antiferromagnetic interactions. Notably, we demonstrated, for the first time, a reversible transition between these two magnetic regimes by controlling the solvation/desolvation of materials, which adjusts the degree of spin frustration without altering the intrinsic spin states. This controllable switching underscores the unique potential of spin-intercalated molecular layered magnets as tunable platforms for studying correlated spin systems. Our findings offer fundamental insights into frustration-driven magnetic phase transitions and pave the way for developing switchable functional materials.

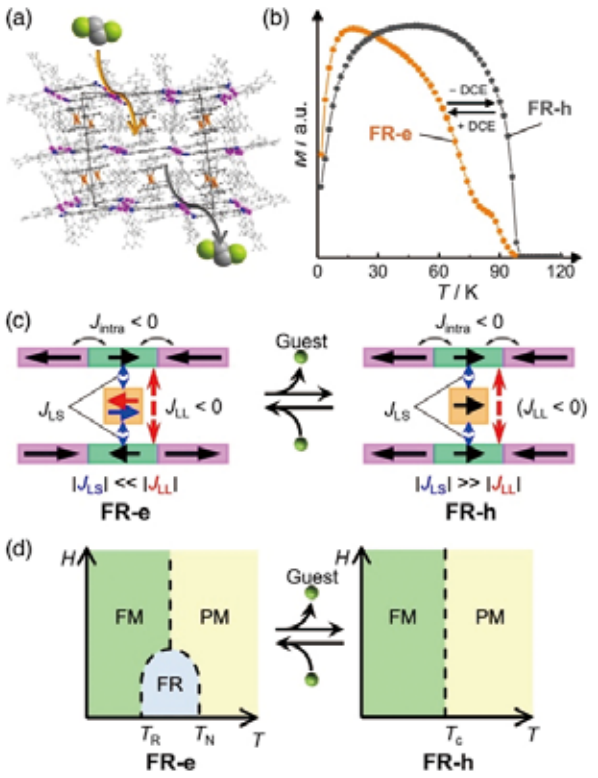

Fig. 1 (a) Structure of spin-intercalated layered MOF and its guest-sorption image. (b) Magnetic properties of FR-e and FR-h phases. (c) Schematic representations of spin arrangements in FR-e and FR-h phases. (d) Phase diagram of FR-e and FR-h phases.

References

[1] H. Fukunaga and H. Miyasaka, Angew. Chem. Int. Ed. **54**, 569 (2015).
[2] H. Fukunaga, W. Kosaka, H. Nemoto, K. Taniguchi, S. Kawaguchi, K. Sugimoto, and H. Miyasaka, Chem. Eur. J. **26**, 16755 (2020).
[3] W. Kosaka, H. Nemoto, K. Nagano, S. Kawaguchi, K. Sugimoto, and H. Miyasaka, Chem. Sci. **14**, 791 (2023).
[4] W. Kosaka, T. Kitayama, C. Itoh, H. Fukunaga, and H. Miyasaka, Cryst. Growth Des. **23**, 1238 (2023).
[5] Q. X. Liu, H. Nemoto, W. Kosaka, and H. Miyasaka, Adv. Sci. **12**, e07957 (2025).

Qingxin Liu, Honoka Nemoto, Wataru Kosaka, and Hitoshi Miyasaka (Solid-State Metal-Complex Chemistry Laboratory)
E-mail: hitoshi.miyasaka.e7@tohoku.ac.jp
URL: https://www.miyasaka-lab.imr.tohoku.ac.jp/cn5/HOME-Eng.html

Giant Tunability of Magnetoelasticity in Fe_4N System as a Platform to Unveil Correlation Between Magnetostriction and Magnetic Damping

Magnetoelastic properties of Fe_4N can be significantly varied by partially replacing Fe with Co or Mn. The high quality Fe_4N film exhibits large negative magnetostriction along the [100] direction (λ_{100}) of -121 ppm while $Fe_{2.3}Co_{1.7}N$ shows λ_{100} of +46 ppm. The correlation between λ_{100} and magnetic damping (α) is also found. Thanks to the tunability and the bipolarity of magnetoelasticity, magnetic nitrides are candidate materials for high-sensitive spintronic strain sensors.

Flexible electronic devices have rapidly become important in the coming trillion-sensor era. As we look at current flexible spintronics, miniaturized strain sensors exploiting the spintronic function have attracted much attention, where the magnetoelasticity linking magnetism and lattice distortion is a vital property for high-sensitive and multi-directional strain detection. Through the inverse magnetostriction effect, the magnetization vector of a magnetic material changes depending on the magnitude and the direction of mechanical stress applied to the magnet. Thus, large magnetoelastic materials and the elucidation of underlying physical mechanism are keys for the development of high-sensitive devices.

Fe_4N, a ferromagnetic iron nitride, exhibits the magnetostriction constant several times larger than that of typical ferromagnetic metals such as Fe, Co, and Ni. In addition, spintronic functions such as tunnel magnetoresistance effect have been reported for the systems with Fe_4N. These features make ferromagnetic nitrides a promising material group not only for spintronic devices, but also for flexible spintronic devices. Thus, it should be clarified to what extend the magnetoelasticity can be enhanced and controlled for the ferromagnetic nitrides in order to achieve best performance of flexible spintronic devices.

We demonstrated that the large negative magnetostriction along [100] (λ_{100}) can be achieved for the high-quality Fe_4N film, which was epitaxially grown employing the rf-assisted molecular beam epitaxy technique, and the value of λ_{100} can be significantly varied by partially replacing Fe with Co or Mn (Fig. 1). The magnitude of λ_{100} was modulated in a wide range from -121 to +46 ppm, indicating the giant tunability and bipolarity of magnetostriction in the ferromagnetic nitride [1].

We also found that the correlation between λ_{100} and magnetic damping experimentally and theoretically. The first-principles calculations revealed that the density of states at the Fermi level [$D(E_F)$] was the leading term to determine the magnitudes for both intrinsic magnetic damping and λ_{100}, suggesting that appropriate control of $D(E_F)$ is indispensable for developing giant magnetoelastic materials. As for the correlation between extrinsic magnetic damping and λ_{100}, the magnetostriction is a source of the two-magnon scattering, resulting in the large extrinsic magnetic damping with increasing λ_{100}. We believe that the findings obtained on the Fe_4N research platform can give a guiding principle for exploring giant magnetoelastic materials, which is applicable to other ferromagnetic systems such as Co-Ni alloys [2].

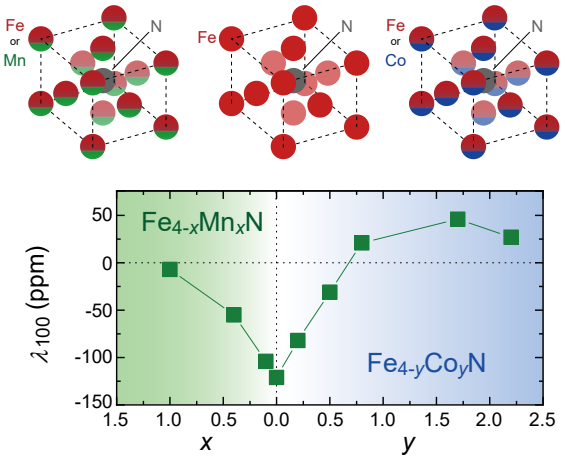

Fig. 1 Crystal structures of magnetic nitrides and the composition dependences of magnetostriction along [100] (λ_{100}) for $Fe_{4-x}Mn_xN$, Fe_4N and $Fe_{4-y}Co_yN$.

References

[1] K. Ito, I. Kurniawan, Y. Shimada, Y. Miura, Y. Endo, and T. Seki, Commun. Mater. **6**, 53 (2025).

[2] I. Kurniawan, K. Ito, T. Seki, K. Masuda, and Y. Miura, Phys. Rev. B **112**, L100407 (2025).

Takeshi Seki (Magnetic Materials Research Laboratory)
E-mail: takeshi.seki@tohoku.ac.jp
URL: https://magmatelab.imr.tohoku.ac.jp/

Machine Learning Prediction of Charged Defect Formation Energies from Crystal Structures

Recent advances in materials informatics have expanded the number of synthesizable materials, but screening candidates such as semiconductors based on defect properties remains difficult. This is largely due to the lack of a general framework for predicting multi-charge defect formation energies from structural data only. We present a general protocol and demonstrate accurate prediction of oxygen-vacancy formation energies in three charge states with a single model. We further introduce a joint machine-learning model combining defect energetics and band-edge predictions for virtual screening. Our protocol is expected to serve as a standard approach for machine-learning studies of point-defect formation energies.

Machine learning (ML) has demonstrated discovery of novel materials, yet their screening has been based on properties of perfect structures. However, defects usually strongly influence performance in materials. For example, deep levels degrade photoabsorbers and native defects often compensate dopants, blocking p- or n-type conduction. While several ML models have predicted formation energies of defects, most require first-principles descriptors [1] or treat only one charge state [2], preventing constructing general ML models using only structures.

To overcome this, we developed a new protocol that predicts various charged defect formation energies in nonmetals using only crystal-structure information [3]. By employing a technique that represents crystal structures as graphs, the method estimates defect formation energies with high accuracy. A key feature is that defects with different charge states can be handled together within a single AI model. For example, the oxygen vacancies examined here can take three charge states in oxides, neutral, +1, and +2, depending on the number of electrons remaining at the vacancy site. By properly incorporating these charge states, we achieved the highest accuracy as a general-purpose defect-prediction model that requires only structural input (Fig. 1). This makes it possible to obtain defect formation energies instantaneously, whereas conventional first-principles calculations used to take several days.

Using this ML model, we searched for p-type semiconductor materials among roughly 2,000 oxide compounds. First, we screened oxides in which hole compensation by oxygen vacancies, one of the main factors that prevents *p*-type behavior in oxides, is unlikely to occur. We then excluded oxides containing toxic or scarce elements. Finally, we computed optical absorption coefficients and hole effective masses through first-principles calculations, and identified promising transparent *p*-type oxides or ambipolar solar-cell absorbers (Fig. 2).

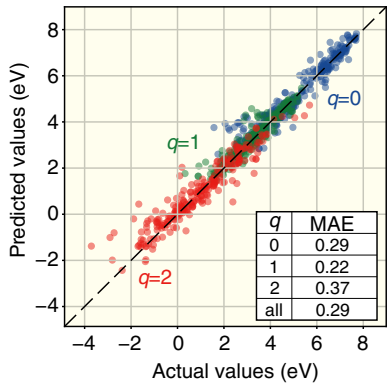

Fig. 1 Parity plots of oxygen vacancy formation energies in neutral, +1 and +2 charge states.

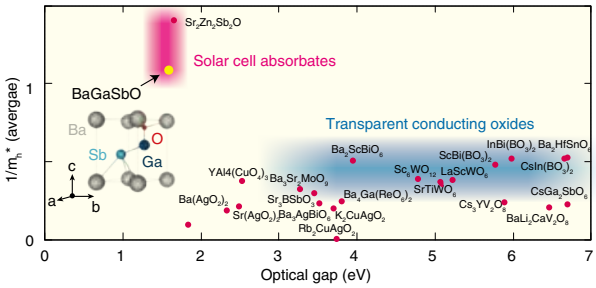

Fig. 2 Reciprocal of the averaged hole effective mass (m_h^*) in units of the free-electron mass plotted against the optical gap for 32 screened oxides.

References

[1] Y. Kumagai, N. Tsunoda, A. Takahashi, and F. Oba, Phys. Rev. Mater. **5**, 123803 (2021).

[2] M. Witman, A. Goyal, T. Ogitsu, A. McDaniel, and S. Lany, Nat Comput. Sci. **3**, 671 (2023).

[3] S. Kiyohara, C. Shibui, S. Bae, and Y. Kumagai, Phys. Rev. Lett. **135**, 246101 (2025).

Yu Kumagai (Multi-Functional Materials Science Research Laboratory)
E-mail: yukumagai@tohoku.ac.jp
URL: https://kumagailab.imr.tohoku.ac.jp/en/

Magnetic Shape Memory Effect in a Heavy Fermion System $CeSb_2$

This study presents a magnetic-field-induced switching of the magnetization easy axis and its memory effect persisting at least up to room temperature in the layered compound $CeSb_2$. This magnetic shape memory effects originate from its unique crystal structure, namely “Ce-pantograph network”.

We report the discovery of a novel magnetic-field-induced switching of the magnetization easy axis and its memory effect, which we call “magnetic shape memory effect”, in the layered rare-earth compound $CeSb_2$ [1].

$CeSb_2$ crystallizes in an orthorhombic structure with nearly equal lattice constants along the in-plane *a* and *b* axes, giving it a pseudo-tetragonal symmetry. At low temperatures, $CeSb_2$ exhibits antiferromagnetic order and a series of metamagnetic transitions when a magnetic field is applied within the crystallographic *ab* plane [2]. Upon applying a sufficiently strong magnetic field (above approximately 30 T far beyond the metamagnetic transition fields 2 T), we observe an abrupt increase in magnetization accompanied by pronounced hysteresis [Fig. 1]. Remarkably, after this high-field process, the direction of the applied magnetic field becomes the new magnetization easy axis, while the perpendicular in-plane direction becomes magnetically hard axis.

Even more strikingly, the magnetization easy axis can be reversibly switched by changing the direction of the applied magnetic field to the other in-plane principal axis. Once induced, the switched magnetic state is retained even after removing the field and remains stable at least up to room temperature. This robustness demonstrates a clear magnetic memory effect, in which the magnetic history of the material is stored in its internal state.

Using polarized light microscopy, we directly visualized the formation of crystallographic domains in as-grown $CeSb_2$ crystals and their rearrangement under high magnetic fields. The easy-axis switching is accompanied by domain reorientation and partial detwinning of the crystal, indicating a strong coupling between magnetic and structural degrees of freedom. From this perspective, the observed phenomenon can be regarded as a magnetic shape memory effect, analogous to martensitic transformations in shape memory alloys but driven by magnetic fields rather than temperature or stress.

We attribute this unique behavior to the characteristic in-plane arrangement of Ce atoms,

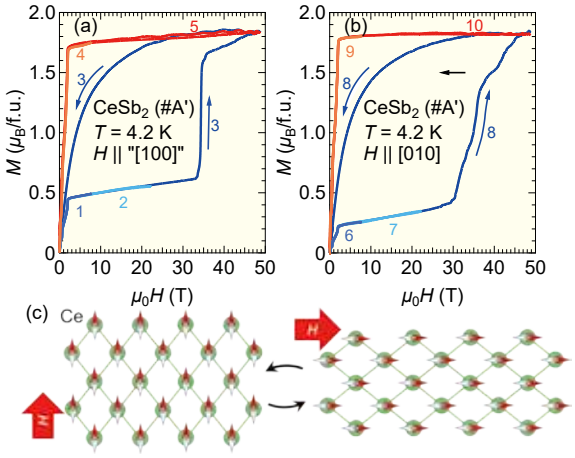

Fig. 1 (a-b) Magnetization curves at 4.2 K. The numbers indicate the order of measurements. (c) The schematic drawings of the field effects on the Ce-pantograph networks.

referred to as the “Ce-pantograph network” [Fig.1(c)]. This network provides a flexible framework that allows subtle structural distortions while preserving interatomic distances, enabling the magnetic anisotropy to be reconfigured by an external magnetic field. The combination of pseudo-tetragonal symmetry, strong magnetic anisotropy, and domain mobility is essential for realizing the easy-axis switching.

Our findings reveal an unprecedented mechanism for controlling magnetic anisotropy through magnetic fields and establish $CeSb_2$ as a new class of magnetic shape memory material. This work opens new avenues for the design of functional magnetic materials with switchable anisotropy and robust memory effects, with potential implications for magnetic devices, sensors, and future spin-based technologies.

References

[1] A. Miyake, R. Hayasaka, H. Fukuda, M. Kondo, Y. Kinoshita, D. X. Li, A. Nakamura, Y. Shimizu, Y. Homma, F. Honda, M. Tokunaga, and D. Aoki, J. Phys. Soc. Jpn. **94**, 043702 (2025).

[2] S. L. Bud’ko, P. C. Canfield, C. H. Mielke, and A. H. Lacerda, Phys. Rev. B **57**, 13624 (1998).

Atsushi Miyake and Dai Aoki (Actinide Materials Science Research Laboratory)
E-mail: atsushi.miyake.b6@tohoku.ac.jp
URL: http://www.imr.tohoku.ac.jp/en/about/divisions-and-centers/research-division/25.html

Research Centers

IMR KINKEN Research Highlights 2026

Quasi-Two-Dimensional Fermi Surfaces Detected by Quantum Oscillations in Ultra-Clean Single Crystal U_2RhIn_8

International Research Center for Nuclear Materials Science

Uranium-based compounds exhibit a variety of exotic phenomena, such as ferromagnetic superconductivity associated with spin-triplet pairing, field-induced superconductivity, and hidden order. The electronic structure—particularly the Fermi surface—plays a crucial role in the emergence of these phenomena. Here, we report the results of quantum oscillation measurements, namely de Haas–van Alphen experiments, performed on the antiferromagnetic heavy-fermion compound U_2RhIn_8 using an ultra-clean single crystal. We directly detect three types of quasi-two-dimensional Fermi surfaces with heavy effective masses, which are in good agreement with band-structure calculations.

Uranium compounds have attracted considerable attention because of their exotic phenomena, such as spin-triplet superconductivity. UTe_2, for example, exhibits field-reentrant superconductivity, in which the upper critical field H_{c2} far exceeds the conventional BCS limit. This behavior strongly suggests the realization of a spin-triplet superconducting state. The existence of multiple superconducting phases observed at high magnetic fields and under pressure further supports this scenario [1]. The electronic structure of UTe_2 consists of two quasi-two-dimensional Fermi surfaces with heavy effective masses, as confirmed by our de Haas–van Alphen (dHvA) experiments [2].

Motivated by these results, we further investigate new materials that may host quasi-two-dimensional Fermi surfaces. Here, we report dHvA measurements on U_2RhIn_8 [3]. This compound belongs to the family of Ce115- and Ce218 heavy-fermion systems, which include heavy-fermion superconductors located near quantum critical points associated with antiferromagnetic fluctuations. Single crystals of U_2RhIn_8 were grown using the self-flux method. The residual resistivity ratio (RRR) reaches 700, indicating the exceptionally high quality of the crystals.

Figure 1(a) shows a typical dHvA oscillation for a magnetic field applied along the *c*-axis in the antiferromagnetic state. The clear oscillations demonstrate the excellent quality of the single crystal. The angular dependence of the dHvA frequencies is presented in Fig. 1(b). As indicated by the green dotted lines, three types of quasi-two-dimensional Fermi surfaces are observed. The corresponding effective masses range from $2m_0$ to $14m_0$, indicating heavy electronic states arising from the contribution of 5*f* electrons to the conduction bands.

Due to the antiferromagnetic order below T_N = 117 K with a propagation vector q = (1/2, 1/2, 0), a magnetic Brillouin zone is formed in the ground state. The corresponding Fermi surfaces within this antiferromagnetic Brillouin zone are schematically illustrated in Fig. 1(c), based on local-density-approximation (LDA) band-structure calculations performed for the antiferromagnetic state. The calculated results are in reasonable agreement with the experimental observations.

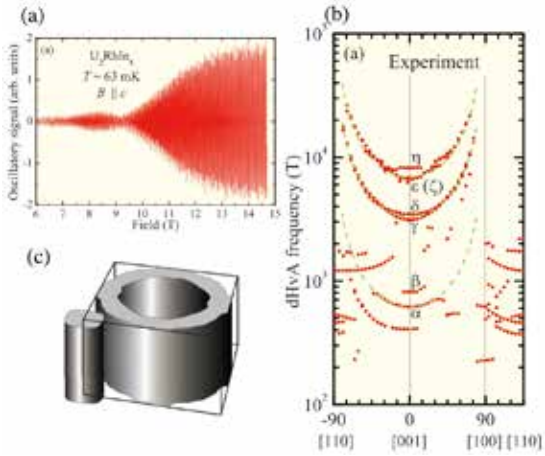

Fig. 1 (a) dHvA oscillations for $H \parallel c$-axis in U_2RhIn_8. (b) Angular dependence of the dHvA frequencies. (c) Schematic illustration of qausi-two-dimensional Fermi surfaces based on the band calculations.

References

[1] T. Vasina, D. Aoki, A. Miyake, G. Seyfarth, A. Pourret, C. Marcenat, M. Amano Patino, G. Lapertot, J. Flouquet, J.-P. Brison, D. Braithwaite, and G. Knebel, Phys. Rev. Lett. **134**, 096501 (2025).

[2] D. Aoki, H. Sakai, P. Opletal, Y. Tokiwa, J. Ishizuka, Y. Yanase, H. Harima, A. Nakamura, D. Li, Y. Homma, Y. Shimizu, G. Knebel, J. Flouquet, and Y. Haga, J. Phys. Soc. Jpn. **91**, 083704 (2022).

[3] D. Aoki, Y. Homma, H. Harima, and I. Sheikin, Phys. Rev. B **111**, 035155 (2025).

Dai Aoki (Head of International Research Center for Nuclear Materials Science)
E-mail: dai.aoki.c2@tohoku.ac.jp
URL: https://www.oarai.imr.tohoku.ac.jp

GIMRT

Fabrication of Bulk-Sized W-1.1%TiC Alloy with Helium Bubble Retention via Powder Metallurgical Route Incorporated with Helium Ambient Mechanical Alloying

International Research Center for Nuclear Materials Science

Transmission electron microscopy observations demonstrated the successful fabrication of bulk-sized W-1.1%TiC alloys containing nanoscale helium bubbles via powder metallurgical route using mechanical alloying under helium atmosphere followed by thermomechanical processing. This fabrication process avoids radioactivation and irradiation-induced defects, thereby facilitating fundamental research into the independent effects of helium bubbles.

Tungsten (W) alloys, promising as materials for plasma facing materials/components in fusion reactors and a target material in high-intensity proton accelerator, suffer from helium (He) embrittlement caused by He bubbles generated in the operating environment.

To investigate the effects of He bubbles on W alloys, high-energy He ion implantation or neutron irradiation are typically performed to produce alloys containing He bubbles. However, these methods introduce irradiation defects in addition to He bubbles, making it difficult to introduce only He bubbles. Furthermore, high-energy irradiation causes the sample to become radioactive. However, we successfully avoided radioactivation using a mechanical alloying method under a He atmosphere to introduce only He bubbles into bulk W-1.1%TiC alloy [1], which is an alloy developed via mechanical alloying and grain-boundary-sliding based microstructural modification to possess a recrystallized nanostructure resistant to embrittlement by recrystallization and/or irradiation [2].

Figure 1 shows the He bubbles observed by TEM. Nano-sized bubbles are observed in the bright-field image (Fig.1a). The weak-beam dark-field image reveals lattice distortion in the matrix surrounding the bubbles, suggesting the presence of internal pressure within the bubbles (Fig.1b). In the HAADF-STEM image (Fig.1c), the bubbles show the dark contrast of the central region due to Z contrast.

This report demonstrates for the first time using advanced TEM that He bubbles can be introduced into bulk W-1.1%TiC without resorting to He ion implantation or neutron irradiation—that is, without inducing radioactivation or irradiation-induced defects—thus contributing to the advancement of He bubble research.

References

[1] T. Sakamoto, K. Yoshida, S. Makimura, H. Noto, E. Wakai, M. Nagae, and H. Kurishita, Vacuum **228**, 113482 (2024).

[2] S. Makimura, H. Kurishita, K. Niikura, H. C. Jung, H. Ishizaki, A. Kimura, M. Onoi, Y. Nagasawa, T. Sakamoto, and H. Ohfuji, Mater. Sci. Forum **1024**, 103 (2021).

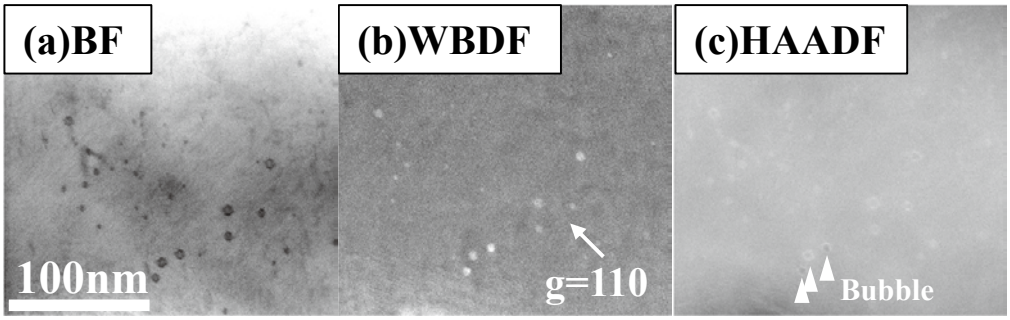

Fig.1 (a) Bright field image, (b) weak beam dark field image, (c) HAADF image in W-1.1%TiC fabricated by mechanical alloying under helium atmosphere.

Tatsuaki Sakamoto (Corresponding Author, Ehime University)
E-mail: sakamoto.tatsuaki.mm@ehime-u.ac.jp
Kenta Yoshida (Corresponding Author, International Research Center for Nuclear Materials Science)
E-mail: kenta.yoshida.d5@tohoku.ac.jp
Dai Aoki (Head of International Research Center for Nuclear Materials Science)
E-mail: dai.aoki.c2@tohoku.ac.jp
URL: https://www.oarai.imr.tohoku.ac.jp

GIMRT

Crystalline Orientation-Dependent AMR Effect in Half-Metallic Ferromagnet of Co_2MnGe Heusler Alloy

Cooperative Research and Development Center for Advanced Materials

Anisotropic magnetoresistance (AMR) and temperature dependence of electronic resistivity were investigated in bulk single crystal of Co_2MnGe. Negative AMR was observed for all crystal orientations, consistent with theoretical predictions for half-metallic ferromagnets. Temperature-dependent resistivity revealed that the absence of electron-magnon scattering and scattering process of $s\uparrow \rightarrow d\downarrow$ further supports the half-metallic nature of Co_2MnGe.

Half-metallic ferromagnets (HMFs) are materials with peculiar density of states (DOS), characterized by the presence of a band gap around the Fermi energy (E_F) in one spin channel. Several Co-based Heusler alloys have been predicted to exhibit Half-metallic (HM) DOS. Anisotropic magnetoresistance (AMR), is an important physical phenomenon in spintronics and the AMR effect originates from the spin-orbit coupling induced by the DOS and anisotropic spin-dependent scattering. According to the extended two-current model of the AMR effect, considering all *s*-*d* electron scattering processes through different spin channels, which has been developed by Kokado *et al.*, the sign of the AMR ratio should always be negative for HMFs [1].

In this study, the crystalline orientation-dependent AMR of Co_2MnGe bulk single crystal was investigated because Co_2MnGe is predicted to be a HMF through theoretical calculations of DOS [2], and experiments by Angular Resolved Photoemission Spectroscopy (ARPES) [3].

A bulk single crystal of Co_2MnGe was grown using the Bridgman method at the CRDAM center.

Figures 1 (a)–(c) show the Laue patterns of bulk single crystal Co_2MnGe in (100), $(0\bar{1}1)$, and $(1\bar{1}1)$ planes, respectively. The crystal structure of $L2_1$-ordered Heusler alloy is indicated in Fig. 1(d) and the specimen was confirmed to have high degree of order ($S = 0.95$). All of the characterizations, including magnetic and electrical resistivity measurements, were also performed using the instruments at the center.

Figure 1(e) shows the relative angle dependence of the AMR of Co_2MnGe measured at 300 K. As shown in the figure, the AMR signs are negative for all crystal orientations. Log(ρ)– Log(T) plot for each crystal orientation is indicated in Fig. 2. It is realized that the electrical resistivity ρ exhibited T-linear dependence and no crystal orientation dependence. T-linear dependence suggests the absence of electron-magnon scattering and scattering process of $s\uparrow \rightarrow d\downarrow$, corresponds to the half-metallic electronic state as well as the negative sign of the AMR [4].

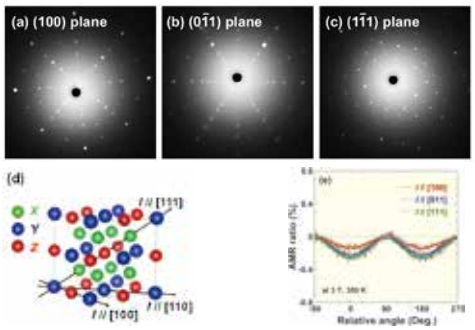

Fig. 1 Laue patterns of (a) (100), (b) $(0\bar{1}1)$, and (c) $(1\bar{1}1)$ planes for Co_2MnGe bulk single crystal. (d) $L2_1$-type ordered structure of X_2YZ Heusler alloy. (e) AMR measured at 300 K in each orientation for Co_2MnGe.

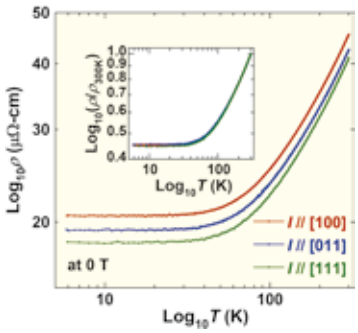

Fig. 2 Log(ρ)– Log(T) plot for each crystal orientation. The values of the electrical resistivity ρ in the inset are normalized as that at 300 K.

References

[1] S. Kokado, M. Tsunoda, K. Harigaya, and A. Sakuma, J. Phys. Soc. Jpn. **81**, 024705 (2012).
[2] S. Ishida, S. Fujii, S. Kashiwagi, and S. Asano,J. Phys. Soc. Jpn. **64**, 2152 (1995).
[3] T. Kono, M. Kakoki, T. Yoshikawa, X. Wang, K. Goto, T. Muro, and R.Y. Umetsu, Phys. Rev. Lett. **125**, 216403 (2020).
[4] T. Tanaka, Y.C. Huang, T. Kubota, S. Kokado, and R.Y. Umetsu, J. Appl. Phys. **138**, 053902 (2025).

Rie Umetsu (Corresponding Author, Cooperative Research and Development Center for Advanced Materials)
E-mail: rie.umetsu@tohoku.ac.jp
Hidemi Kato (Head of Cooperative Research and Development Center for Advanced Materials)
E-mail: hidemi.kato.b7@tohoku.ac.jp
URL: https://www.crdam.imr.tohoku.ac.jp/english/

GIMRT

Advanced Cu-Nb/Nb_3Sn Wire Development for 33T Cryogen-Free Superconducting Magnets

High Field Laboratory for Superconducting Materials

Nb_3Sn wires reinforced with Nb-rod method Cu-Nb exhibit excellent superconducting properties under stress. For the 33 T cryogen-free superconducting magnet (33T-CSM) under development at Tohoku University, we designed a high-strength, high-I_c wire based on the Cu-Nb/Nb_3Sn wire used in the 25 T cryogen-free magnet. Enhancements include increasing the Cu-Nb reinforcement fraction from 35% to 38%, Nb content from 20% to 25%, and modifying the bronze composition to Cu-15.7 wt% Sn-0.3 wt% Ti. These changes improved strength and I_c, allowing the wire to maintain critical current density without degradation up to 345 MPa, exceeding the 275 MPa tensile stress expected in 33T-CSM.

Nb_3Sn wires reinforced using the Nb-rod method Cu–Nb enable compact high-field superconducting magnets with high hoop-stress designs. CuNb/Nb_3Sn Rutherford cables have been used in the 14 T low-temperature superconducting (LTS) outsert of the 25 T cryogen-free superconducting magnet (25T-CSM) at HFLSM, which has been operated as a user magnet for more than 10 years. In this study, we improved the mechanical strength of CuNb/Nb_3Sn wires for the 33T-CSM by increasing the CuNb volume fraction from 35% to 38% and the Nb content in CuNb from 20% to 25%. In addition, the Sn content in the bronze matrix was increased from 14 wt% to 15.7 wt% to enhance the non-Cu J_c [1].

Figure 1 shows cross-sectional views of the newly developed CuNb/Nb_3Sn strand and the corresponding Rutherford cable. The outer diameter of the strands is 0.8 mm. The Rutherford cable consists of 16 CuNb/Nb_3Sn strands, as shown in the lower part of Fig. 1. Two different heat-treatment conditions were adopted to obtain different I_c grades.

As a result, both the electromechanical performance (I_c-stress) and I_c were improved compared with those of the 25T-CSM conductor as shown in Fig. 2. The I_c values were maintained under high stresses up to 345 MPa, with a high irreversible stress limit of about 530 MPa. Thanks to the high performance of the advanced CuNb/Nb_3Sn Rutherford cable, A 14 T LTS outsert with a 320 mm bore was developed for the 33T-CSM, with a maximum hoop stress of 275 MPa. Nominal-stress operation was successfully achieved under cryocooled conditions [2]. The 33T-CSM, combined with a 19 T REBCO insert, will be completed in 2027.

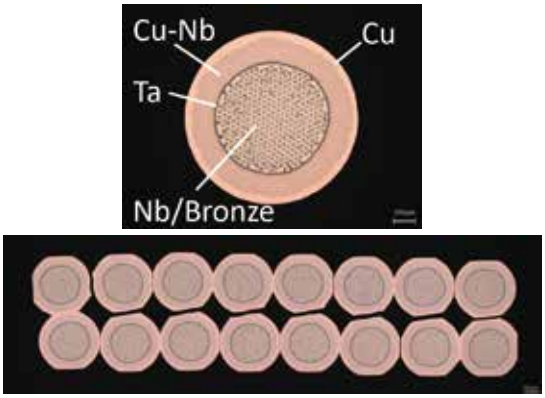

Fig. 1 Cross-sections of newly developed CuNb/Nb_3Sn strand (top) and Rutherford cable (bottom).

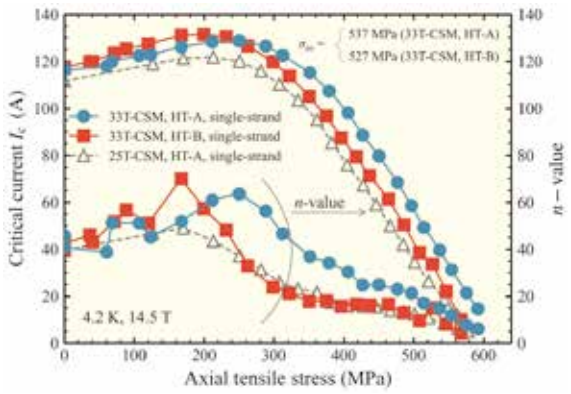

Fig. 2 Axial tensile stress dependence of critical current and n-value for CuNb/Nb_3Sn strands for 33T-CSM and 25T-CSM [1].

References

[1] R. Taniguchi, M. Sugimoto, H. Fukushima, K. Nakao, K. Hirose, S. Awaji, and H. Oguro, IEEE Trans. Appl. Supercond. **35**, 6001605 (2025).

[2] S. Awaji et al, IEEE Trans. Appl. Supercond. **35**, 4300406 (2025).

Ryo Taniguchi (Corresponding Author, Furukawa Electric Company Ltd.)
E-mail: ryo.taniguchi@furukawaelectric.com
Satoshi Awaji (Head of High Field Laboratory for Superconducting Materials)
E-mail: awaji@tohoku.ac.jp
URL: https://www.hflsm.imr.tohoku.ac.jp/

Local Structural Analysis of Zr-Based Functional Oxides for High-Temperature Energy Conversion

Collaborative Research Center on Energy Materials

Zr-based oxides play an essential role in high-temperature energy conversion systems, such as Solid Oxide Fuel Cells (SOFCs) and Solid Oxide Electrolysis Cells (SOECs), due to their high chemical stability and ionic conductivity. Their performance depends heavily on the local structure of the oxides, including the defect structures. Local structure analysis, which combines advanced spectroscopic techniques with Density Functional Theory (DFT) calculations, provides new material designs for proton-conducting barium zirconates and Sc-stabilized zirconia oxide-ion conductors.

Y- and Yb-doped barium zirconate (BCZYY) is a promising electrolyte for intermediate-temperature fuel cells and electrolyzers; however, it suffers from poor sinterability. To overcome this, transition metal oxides, such as copper oxide (CuO), are added as sintering aids; however, the mechanism by which these aids degrade proton conductivity remains unclear. Our group has investigated the sintering mechanism and dissolution state of Cu using Electron Spin Resonance (ESR) spectroscopy [1]. A critical finding from the ESR analysis was that the dopant did not substitute the Zr/Ce site but dissolved into interstitial sites, adopting a 4-fold coordination (Fig. 1). To maintain electrical neutrality, the presence of interstitial Cu ions induces Ba deficiency. Consequently, this reduces the effective concentration of oxygen vacancies available for the hydration reaction, thereby decreasing proton conductivity.

Sc-stabilized zirconia (ScSZ) exhibits superior ionic conductivity compared to YSZ; however, it suffers from conductivity degradation during long-term operation. While alumina (Al_2O_3) doping is known to suppress this degradation, the microscopic mechanism and the exact state of Al within the lattice are not well understood. Our group has also conducted a detailed analysis of the local structure of Al in ScSZ using solid-state NMR spectroscopy and DFT calculations [2]. The study revealed that despite the significantly smaller ionic radius of Al than that of Zr, Al occupies 6-, 7-, and 8-coordinated states, depending on the configuration of the surrounding oxygen vacancies. A notable discovery is that the 7- and 8-coordinated Al species adopt a locally "effective 4-coordinated" (tetrahedral-like) structure (Fig. 2). This unique local distortion arises to accommodate the size mismatch between the small Al ion and the large Zr site. This mechanism effectively suppresses the phase transition and oxygen vacancy ordering, which leads to conductivity degradation.

These findings highlight the critical importance of understanding the local structure, which cannot be fully captured by average crystal structure analysis, in improving the performance of Zr-based functional oxides [3].

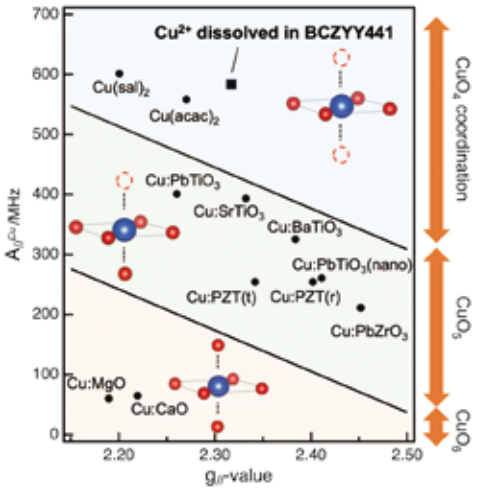

Fig. 1 $g_{//,zz}$ vs. $A_{//Cu,zz}$ spin-Hamiltonian parameter for various Cu^{2+} centers, in which the ESR data of Cu-added BCZYY heat-treated at 900 °C and those of Cu in various oxides are plotted.

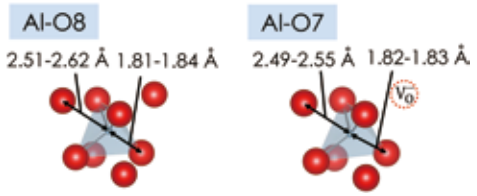

Fig. 2 Local structure of Al in ScSZ.

References

[1] Y. Unaki, H. Kawamori, S. Kobayashi, N. Osada, A. Ishii, I. Oikawa, and H. Takamura, J. Mater. Chem. A **13**, 30427 (2025).

[2] I. Oikawa, A. Fujimaki, A. Ishii, F. Tamazaki, H. Okamoto, and H. Takamura, Solid State Ionics **430**, 116997 (2025).

[3] Y. Okazaki, A. Ishii, I. Oikawa, and H. Takamura, Small **21**, 2412830 (2025).

Hitoshi Takamura (Corresponding Author, Collaborative Research Center on Energy Materials)
E-mail: hitoshi.takamura.a8@tohoku.ac.jp
Tetsu Ichitsubo (Head of Collaborative Research Center on Energy Materials)
E-mail: tichi@tohoku.ac.jp
URL: https://www.imr.tohoku.ac.jp/en/about/divisions-and-centers/facilities/05.htm

GIMRT International Co-Authored Paper

Exploring Transition Metal High Entropy Alloys from First-Principles and Machine Learning with Data Augmentation

Center for Computational Materials Science

We applied first-principles calculation combing the elemental convolution graph neural networks for exploring new compositions of transition metal high entropy alloys (HEAs) with superior physical property. Data augmentation using both the generative AI (GAN) and the physical method of cluster expansion (CE) are cooperated to enhance the small DFT dataset, for expanding the searching space and improving the prediction accuracy.

This research series was started from two quinary high entropy alloys (HEAs), the Cantor alloy FeCoNiCrMn, and the FeNiCoCrPd which is synthesized by intentionally substituting Mn in Cantor alloy with Pd, and this new HEA was reported to be achieved 2 times higher strength than Cantor alloy. We investigated the stability and structural properties of these two HEAs based on first-principles calculation using the special quasi-random structures (SQS) models, and revealed the mechanism of Pd enhancement of the mechanical properties with substitution Mn, and the balance between inhomogeneous and stability as the key for exploring the new HEAs [1-2]. Based on about 1,100 DFT SQS data on these 2 HEAs including all their sub-systems (binary, ternary, quaternary) in fcc, bcc and hcp structures, we developed a deep learning model of elemental convolution graph neural networks (ECNet) in cooperating with transfer learning, from which three new compositions of $(FeCoNiCrMn)_{1-x}Pd_x$ with superior mechanical property to known HEAs have been discovered [3]. For further exploring new compositions in a wider searching space, we challenged the data augmentation based on our DFT dataset using the generative AI (GAN) [4] and the physical method of cluster expansion (CE) [5] in parallel. A new generative network framework (EFTGAN) improved the performance of prediction model in a small dataset and predicted the concentration dependent formation energies, square root mean displacements (RMSDs) and magnetic moments in $(FeCoNiCrMn)_{1-x}Mn_x/Pd_x$. Especially, this model addresses the complexity of the graph neural network inputs by generating elemental features instead of direct computational structures as inputs, enabling fast and accurate large-scale prediction of HEAs. Meanwhile, the generalized cluster expansion method has been applied to the original DFT dataset to create a large amount of pseudo-DFT data, and during the cluster expansion process, the physical properties of the clusters are extracted through sets of the effective cluster interactions (ECIs). Such physical knowledge helps to figure out particularly important atomic pairs and groups as sub-spaces in the high dimensional exploring space, leading to more effective and physically meaningful prediction. Fig.1 shows one section of prediction on temperature dependent formation free energies and magnetic moments for a complicated composition of a quinary HEA which is hinted from the pair interaction energies features. Our works facilitate the understanding on the complex relation among composition-structure-properties of materials, provide an effective approach to overcome the small dataset problem in applying to the complicated material systems [4].

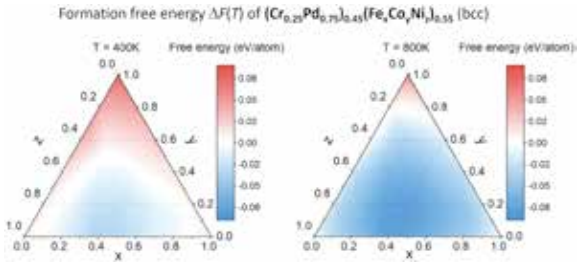

Fig. 1 The prediction of formation energies and magnetic moments for (Cr, Pd)-($Fe_xCo_yNi_z$). This composition is hinted by attractive feature among Fe-Co-Ni atomic pairs and repulsive interaction between Cr-Pd pairs [4].

References

[1] N. -D. Tran, A. Saengdeejing, and Y. Chen, J. Phase Equilib. Diffus. **42**, 606 (2021).

[2] N. -D. Tran, T. Davey, and Y. Chen, J. Appl. Phys. **133**, 045101 (2023).

[3] X. Wang, N. -D. Tran, S. Zeng, C. Hou, Y. Chen, and J. Ni, Npj Comput. Mater. **8**, 253 (2022).

[4] Y. Sun, C. Hou, N. -D. Tran, Y. Lu, Z. Li, Y. Chen, and J. Ni, Npj Comput. Mater. **11**, 54 (2025).

[5] Z. Li, N. -D. Tran, Y. Sun, Y. Lu, C. Hou, Y. Chen, and J. Ni, J. Mater. Chem. C **13**, 17601 (2025).

Ying Chen (Corresponding Author, Global Learning Center, Tohoku University)
E-mail: ying.chen.c1@tohoku.ac.jp
Momoji Kubo (Head of Center for Computational Materials Science)
E-mail: momoji@tohoku.ac.jp
URL: https://www.sc.imr.tohoku.ac.jp/eng/

International Co-Authored Paper

Complementary Neutron and Synchrotron Approach for Investigating the Origin of Super-Elinvar Characteristics in FeMn Based Alloys

Quantum Beam Center for Materials Research

Elinvar characteristics have strong potential for applications in precision sensors and structural components that require dimensional or mechanical stability against thermal variations. Recently, non-magnetic alloys have been reported to exhibit Invar and Elinvar properties superior to conventional ferromagnetic alloys. Such materials are attractive for use in magnetic-field environments; however, the mechanisms responsible for these properties have remained unclear. In this study, we clarify the role of structural transformations and associated lattice instability in the emergence of Elinvar characteristics in FeMn based alloys, using complementary neutron and synchrotron scattering techniques.

Fe–25Mn–3Mo is a Super-Elinvar alloy [1], an antiferromagnetic material that exhibits extremely small temperature coefficients of elastic properties over a wide temperature range. Because large and uniform magnetostrictive strains are generally not expected in antiferromagnetic systems, the origin of this behavior remains unclear. Moreover, this alloy simultaneously displays Invar characteristics over the same temperature range. Such coexistence cannot be explained by the conventional magnetovolume effect associated with ferromagnetic transitions, as the conditions optimizing spontaneous magnetostriction differ between Invar and Elinvar phenomena. To clarify the origin of the Super Elinvar behavior, we focused on the fcc–hcp martensitic transformation and the associated structural instabilities and local strains [2].

As shown in Fig. 1(a) and (b), Temperature-dependent neutron diffraction measurements using HERMES at JRR-3 revealed that the temperature range exhibiting Elinvar behavior coincides with the coexistence region of the parent fcc phase and the hcp martensitic phase. In this mixed phase regime, structural instability in the remaining parent fcc phase is expected to reduce the elastic modulus and contribute to the macroscopic elastic response. Because conventional macroscopic or ultrasonic measurements are challenging under such two-phase coexistence, reciprocal space phonon measurements offer a more suitable approach. Due to the difficulty of growing large, high quality single crystals in eutectic systems, we performed high-resolution inelastic X-ray scattering (IXS) experiments using mm-sized single crystals grown by the Bridgman method at BL43LXU of the RIKEN SPring-8 Center. As shown in Fig. 1 (c), TA phonon has softening with decreasing temperature, accompanied by deviations from linear dispersion ($\hbar\omega \propto q$) near the Γ point, indicating anharmonicity of long wavelength limit.

In addition, pair distribution function analyses via neutron total scattering showed that nearest-neighbor contraction is most pronounced in the Elinvar temperature range. Since Young's modulus reflects the curvature of the interatomic potential, such local structural deviations significantly influence the macroscopic elastic response. Collectively, these results demonstrate that local structural fluctuations associated with the fcc–hcp transformation, along with long wavelength phonon softening, are key factors underlying the Super Elinvar characteristics in Fe–25Mn–3Mo.

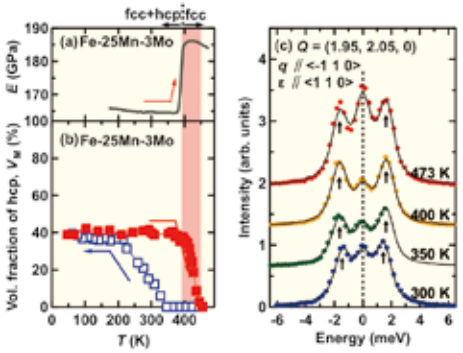

Fig. 1 (a) Heating curve of Young's modulus E [1]. (b) Volume fraction of the martensite (hcp) phase V_M. The filled red and open blue rectangles show results on warming and cooling, respectively. (c) IXS spectra of the Fe-25Mn-3Mo single crystal sample measured at different temperatures ($\boldsymbol{q}$: propagation wave vector, ε: atomic displacement direction). The solid lines represent the results of a fit using three Lorentzian components with resolution convolution. Black arrows denote the positions of the inelastic scattering peaks.

References

[1] T. Masumoto, S. Ohnuma, K. Sugawara, and H. Kimura, Mater Trans. **58** (4), 701 (2017).

[2] Y. Umemoto, Y. Ikeda, T. Honda, D. Ishikawa, J. A. Schneeloch, J. C. Neuefeind, S. Tozawa, R. Umetsu, D. Louca, A. Q. Baron, and M. Fujita, Sci. Technol. Adv. Mater. **26** (1), (2025).

Yoshihiko Umemoto (Corresponding Author, Oak Ridge National Laboratory)
E-mail: umemotoy@ornl.gov
Masaki Fujita (Corresponding Author, Quantum Beam Materials Physics Research Laboratory)
E-mail: masaki.fujita.b5@tohoku.ac.jp
Rie Umetsu (Head of Quantum Beam Center for Materials Research)
E-mail: rie.umetsu@tohoku.ac.jp
URL: https://gimrt.www.imr.tohoku.ac.jp/en/research/qbcmr.html

International Co-Authored Paper

Synthetic Antiferromagnet Spintronics

International Collaboration Center (ICC-IMR)

We investigate the dynamics of bimerons and skyrmions in synthetic antiferromagnets. Synthetic antiferromagnets are advantageous for decreasing the bimeron and skyrmion Hall angles and enabling texture detection through local magnetization, bypassing the need to rely on the Neel order parameter. Using micromagnetic simulations and Thiele's equation approach we calculated the bimeron/skyrmion Hall angles.

Motivated by the differences between of skyrmions and their in-plane magnetized analogues – bimerons – in synthetic antiferromagnets (SAFs), we investigated their current-driven dynamics employing micromagnetic simulations and analytical Thiele's equation approach. We considered SAF structures consisting of several antiferromagnetically coupled layers. For bimerons, we considered additional ferromagnetic layers with fixed in-plane magnetization adjoined to the SAF, see Fig. 1.

In this case, the effect of exchange bias from the fixed layer is similar to a magnetic field, i.e., increasing the strength of exchange bias reduces the bimeron's size in the adjacent layer. This translates through the rest of SAF via interlayer antiferromagnetic exchange. Since the strength of the exchange bias can be modified by changing interlayer exchange coupling between a fixed layer and the SAF, this configuration offers additional control over the size of the spin texture and its motion. However, since this effect diminishes with distance from the fixed layer, bimerons are smaller at the bottom and become larger at the top layers of the SAF. To prevent this asymmetry and increase the number of layers where the bimeron size is controlled by this effect, we also considered a configuration with the second fixed layer added on top of the SAF.

We have shown that in the uncompensated SAFs, bimeron and skyrmion Hall effects diminish in the bulk limit, which can be understood by the decrease in the averaged topological charge with increasing the number of layers. However, bimeron/skyrmion Hall angles have a quite nonmonotonic dependence on number of layers N with an extremum for a certain N. The bimeron (skyrmion) Hall effect vanishes for compensated SAFs with two fixed layers, whereas the SAFs with only one fixed layer exhibit nonzero Hall angles, which becomes more evident when interlayer exchange interaction is weak. Remarkably, we identified the conditions when bimerons and skyrmions in uncompensated SAFs

Fig. 1 Schematic representation of a 5-layer SAF for bimerons stabilization with one fixed layer.

can move faster than in antiferromagnets. Depending on spin-transfer torque strength, spin texture velocities in uncompensated SAFs increase or decrease with the number of layers. Finally, we have studied finite temperature effects on bimeron and skyrmion dynamics and stability in SAFs by employing stochastic Landau-Lifshitz-Gilbert equation with white-noise correlated random magnetic fields. Our findings offer a comprehensive understanding of the topological magnetic texture dynamics in SAFs, which is essential for designing topological spin-texture based logic and memory nanodevices.

Furthermore, the interplay of these spin textures with spin-orbit coupled substrates [1] would be interesting to study as well in SAFs, since the previous studies mainly focused on the Hall responses of skyrmions coupled to heavy-metal substrates. Finally, this study can be extended to the investigation of domain-wall bimerons [2] and their dynamics in synthetic antiferromagnets. These findings will deepen the understanding of SAF dynamics and offer guidance for their implementation in skyrmion- and bimeron-based spintronic devices.

References

[1] Z. Llewellyn, E. Mascot, O. A. Tretiakov, and S. Rachel, Phys. Rev. B **112**, 155417 (2025).

[2] J. Chen, X. Li, L. Shen, Z. Wang, H. Zhang, A. Litvinenko, J. Åkerman, X. Xu, O. A. Tretiakov, and Y. Zhou, Phys. Rev. B **112**, 224420 (2025).

Oleg A. Tretiakov (Corresponding Author, University of New South Wales)
E-mail: o.tretiakov@unsw.edu.au
Hiroyuki Nojiri (Head of International Collaboration Center)
E-mail: hiroyuki.nojiri.e8@tohoku.ac.jp
URL: https://www.icc-imr.imr.tohoku.ac.jp/

Derivation of a Scaling Law for the Supercurrent Rectification Effect

Laboratory of Low Temperature Materials Science

Supercurrent rectification effect in superconductors with broken inversion symmetry has attracted growing interest. Here, we report on a universal scaling law for nonreciprocal transports, which is derived from the comparative study of the superconducting diode effect and nonreciprocal resistance in a superconducting Fe(Se,Te)/FeTe heterostructure. Our findings pave the way for functionalizing superconducting diode devices.

Nonreciprocal response of superconducting properties has attracted growing interest from the viewpoint of not only its fundamental mechanism but also its application as an ideal diode. A superconducting thin-film heterostructure with structural inversion asymmetry is a promising platform for observing it. One of the archetypal phenomena is the nonreciprocal resistance $R=R_0(1+\gamma BI)$ described with the nonreciprocal coefficient γ, where the resistance R in one direction of current I (or magnetic field B) is larger than that in the opposite direction in the superconducting transition regime [1]. The other is the superconducting diode effect described with the efficiency $\eta=(I_c^+-I_c^-)/(I_c^++I_c^-)$, where the critical current in one direction I_c^+ is larger (or smaller) than that in the opposite direction I_c^- [2]. In most cases, the supercurrent rectification effects have been discussed by measuring either γ or η, in spite that both should be related parameters. Therefore, it has been highly desired to clarify the correlation between γ and η with systematic measurements in the same system.

Here, we studied the nonreciprocal superconducting transport properties in a Fe(Se,Te)/FeTe heterostructure device (Fig. 1(a)), where the inversion symmetry is broken along the out-of-plane direction [3]. The large critical current and the high upper critical field, as well as the enhanced spin–orbit interaction in this system make it possible to measure both γ and η in one sample. Then, we succeeded in observing the large γ enhanced in the superconducting transition regime and the large η up to 15% in superconducting regime (Fig. 1(b)) in a wide range of temperature T and in-plane B. Furthermore, by comparing γ and η as a function of T and B, we found a universal scaling between them (Fig. 2).

The successful scaling relation shown in Fig. 2 can be understood comprehensively using the asymmetric pinning potential for vortices, which is induced by the Rashba spin–orbit interaction originating from the inversion symmetry breaking. Our demonstration of the unified picture for superconducting rectification effect sheds light on perspectives for material selection and structural design toward highly efficient supercurrent rectification devices.

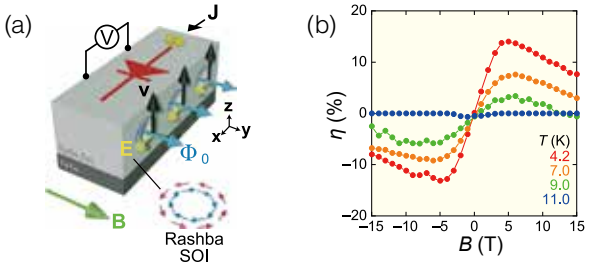

Fig. 1 (a) A schematics of Fe(Se,Te)/FeTe heterostructure and superconducting diode effect in the presence of quantum vortices. (b) The magnetic-field dependence of superconducting diode efficiency η.

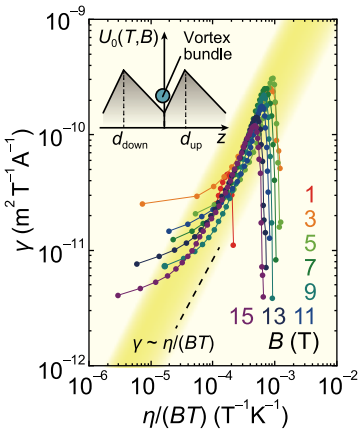

Fig. 2 The scaling relationship between the nonreciprocal coefficient γ and η/BT for B = 1 to 15 T obtained empirically. (Inset) Schematic of asymmetric pinning potential.

References

[1] Y. M. Itahashi, T. Ideue, Y. Saito, S. Shimizu, T. Ouchi, T. Nojima, and Y. Iwasa, Sci. Adv. **89**, eaay9120 (2020).

[2] F. Ando, Y. Miyasaka, T. Li, J. Ishizuka, T. Arakawa, Y. Shiota, T. Moriyama, Y. Yanase, and T. Ono, Nature **584**, 373 (2020).

[3] Y. Kobayashi, J. Shiogai, T. Nojima, and J. Matsuno, Commun. Phys. **8**, 196 (2025).

Tsutomu Nojima (Corresponding Author, Laboratory of Low Temperature Materials Science)
E-mail: t.nojima@tohoku.ac.jp
Takahiko Sasaki (Head of Laboratory of Low Temperature Materials Science)
E-mail: takahiko.sasaki.d3@tohoku.ac.jp
URL: https://ltsd.imr.tohoku.ac.jp/index-e.html

Effects of Irradiation on Interfacial Strength and Microstructure of Double-Layer Mullite and Alumina Coating on SiC

Laboratory of Alpha-Ray Emitters

Silicon carbide (SiC) ceramics hold significant potential for application in nuclear reactor components due to properties such as high-temperature strength and low activation. This study sought to clarify the effects of irradiation on the interfacial strength of multilayer coatings consisting of an SiC base layer, a mullite bond layer, and an alumina top layer on an SiC substrate deposited using CVD.

The Laboratory of Alpha-Ray Emitters comprises three chemistry and three physics laboratories capable of handling approximately 190 distinct radioisotopes and nuclear fuel materials. As a premier national shared-use facility, we conduct cutting-edge research ranging from the physicochemical properties of actinide compounds to irradiation effects on nuclear fission and fusion reactor materials. In recent years, the laboratory has established itself as a key domestic supplier of Actinium-225 (Ac-225), an isotope attracting global attention for its potential in Targeted Alpha Therapy. Furthermore, we provide a seamless research environment covering everything from material synthesis to measurement. Our extensive infrastructure includes tetra-arc furnaces, Physical Property Measurement Systems (PPMS), nanoindenters, Focused Ion Beam (FIB) systems, and Transmission Electron Microscopes (TEM). In this article, we present research findings achieved at this laboratory regarding Silicon Carbide (SiC), a material garnering attention for its potential use in nuclear applications.

Silicon carbide ceramics hold significant potential for application in nuclear reactor components due to properties such as high-temperature strength and low activation. However, despite their inherent corrosion resistance in severe environments, their corrosion rate accelerates under neutron irradiation. Although a double-layer ceramic coating - comprising a mullite bond coat and an alumina topcoat deposited on SiC via Chemical Vapor Deposition (CVD) - has demonstrated superiority over single-layer alumina coatings, its stability under irradiation remains to be elucidated. This study sought to clarify the effects of irradiation on the interfacial strength of multilayer coatings consisting of an SiC base layer, a mullite bond layer, and an alumina top layer on an SiC substrate deposited using CVD. Irradiation experiments were conducted at 300 °C with 5.1-MeV Si ions up to 10 displacements per atom. To assess the interfacial strength, a novel testing method, called the double-notch shear compression testing method, was developed based on ASTM standards and was implemented using a nanoindenter. In this study, because of the limited irradiation volume, the interfacial strength was measured using the double-notch shear testing method, as shown in Fig. 1. The micropillars were fabricated using a focused ion beam (FB-2100, Hitachi), with each interface positioned centrally. The results showed an increase in the interfacial strength at the SiC/mullite and alumina/mullite interfaces with irradiation. Microstructural analysis of the fracture surface through scanning electron microscopy–energy-dispersive X-ray spectroscopy revealed that cracks propagated within the mullite layer, indicating the presence of mullite on the fracture surface. Transmission electron microscopy (TEM) images indicated that a 2 μm thick transition layer existed at the SiC/mullite interface but not at the alumina/mullite interface. The TEM electron energy loss spectroscopy suggested that the Al-O bonding structures in the transition layer were changed from tetrahedral (AlO_4) to octahedral (AlO_6) through irradiation, and this structural transition may directly affect the strength.

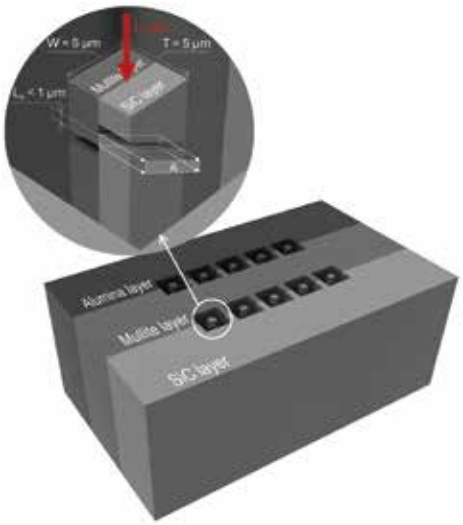

Fig. 1 Schematic of the micropillars fabricated on each interface and the dimensions of the micropillars [1].

References

[1] T. Miyagishi, S. Kondo, H. Katsui, K. Yabuuchi, R. Usukawa, Y. Ogino, H. Yu, and R. Kasada, J. Nucl. Mater. **603**, 155410 (2025).

Kiyohiro Yabuuchi (Head of Laboratory of Alpha-Ray Emitters)
E-mail: kiyohiro.yabuuchi.a7@tohoku.ac.jp
URL: https://alpha.imr.tohoku.ac.jp/en.html

Factors Governing Time-Dependent Hydrogen Charging Behavior Revealed by Ion Chromatography

Analytical Research Core for Advanced Materials

This study demonstrates that electrochemical hydrogen charging in NaCl solutions containing NH_4SCN remains stable at moderate cathodic potentials but becomes unstable at highly negative potentials. The instability results from changes in solution chemistry, particularly the decomposition of SCN^- and the pH decrease caused by counter-electrode reactions, which together influence hydrogen absorption.

Hydrogen embrittlement is a critical issue for metallic materials, particularly steels, as it degrades mechanical properties and can lead to unexpected failure. Electrochemical hydrogen charging using NaCl aqueous solution containing NH_4SCN is widely employed to simulate hydrogen uptake, because NH_4SCN effectively promotes hydrogen absorption [1, 2]. However, under long-term charging, changes in solution chemistry may occur, potentially compromising the stability and reproducibility of hydrogen charging. Therefore, in this study, the stability of electrochemical hydrogen charging to iron in a NaCl aqueous solution containing NH_4SCN was investigated using electrochemical hydrogen permeation tests, with focus on how solution chemistry changes and affects hydrogen absorption behavior [3]. Special attention was paid to the role of electrochemical reactions occurring during prolonged hydrogen charging.

The hydrogen absorption behavior was measured using electrochemical hydrogen permeation tests. At potentials between –0.9 V and –1.3 V (All potentials are referred to Ag/AgCl (3.33 M KCl)), the hydrogen absorption rate remained stable, indicating suitable conditions for consistent hydrogen charging. Under these conditions, the more negative the potential, the higher the absorption rate. In contrast, at –1.6 V, the hydrogen absorption rate fluctuated significantly over time, showing an initial increase in permeation current followed by a decrease, as shown in Fig. 1(b). This behavior indicates a loss of hydrogen uptake stability under severe cathodic conditions.

A detailed analysis of the hydrogen-charging solution was conducted using ion chromatography. During hydrogen charging at –1.6 V, the pH near the specimen decreased substantially over time, while SCN^- concentration decreased and SO_4^{2-} concentration increased as shown in Fig. 1c-e. These changes are linked to oxidation reactions of SCN^- at the counter electrode, which produce protons and sulfate species,

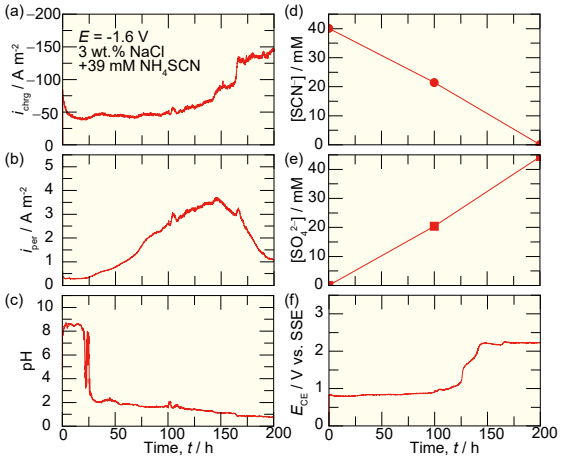

Fig. Transients of (a) hydrogen charging current density, (b) hydrogen absorption current density, (c) pH, and concentrations of (d) SCN^- and (e) SO_4^{2-}, and potential of counter electrode during hydrogen charging at -1.6 V in a NaCl aqueous solution containing 39 mN NH_4SCN.

lowering the pH and consuming SCN^-. This altered the solution chemistry, enhancing hydrogen absorption initially (due to lower pH) but later weakening it as SCN^-, which promotes hydrogen uptake, was depleted. The results highlight the strong influence of counter-electrode reactions on the hydrogen charging environment.

In conclusion, stable electrochemical hydrogen charging in NaCl with NH_4SCN is achieved at moderate potentials (–0.9 to –1.3 V), whereas at more negative potentials (–1.6 V), changes in solution chemistry undermine stability, primarily due to proton generation and SCN^- depletion.

References

[1] E. Akiyama and S. Li, Corrosion Reviews **34**, 103 (2016).
[2] S. Ajito, T. Hojo, M. Koyama, and E. Akiyama, ISIJ Int. **61**, 1209 (2021).
[3] S. Ajito, Y. Kabasawa, H. Kakinuma, M. Koyama, and E. Akiyama, Corrosion Science **249**, 112843 (2025).

Saya Ajito (Corresponding Author, Environmentally Robust Materials Research Laboratory)
E-mail: saya.ajito.d1@tohoku.ac.jp
URL: http://www.imr.tohoku.ac.jp/en/about/divisions-and-centers/research-division/12.html
Eiji Akiyama (Head of Analytical Research Core for Advanced Materials)
E-mail: eiji.akiyama.d1@tohoku.ac.jp
URL: https://www.imr.tohoku.ac.jp/en/about/divisions-and-centers/service-divisions/03.html

Materials Science in Action: From Bronze Mirrors to Heritage Research

Innovative Knowledge Hub for Humanities and Materials Science

IKH advances materials-based research on cultural and natural heritage through non-destructive, complementary analytical techniques. Interdisciplinary projects, including bronze mirror studies and heritage conservation research, extend the application of materials science methods and develop transferable analytical approaches for heritage-related materials.

The Innovative Knowledge Hub for Humanities and Materials Science (IKH) was launched in 2023 at the Institute for Materials Research (IMR), Tohoku University, with support from the Ministry of Education, Culture, Sports, Science and Technology (MEXT), under the Promotion of Development of a Joint Usage/Research System Project. Conceived as a ten-year initiative through FY2033, IKH aims to promote the mutual development of the humanities and materials science by fostering a nationwide interdisciplinary research community. A core function of IKH is its Liaison activity, which facilitates access to analytical infrastructure and connects humanities researchers with materials scientists and research facilities.

In 2025, IKH activities were integrated with the Global Institute for Materials Research Tohoku (GIMRT) through dedicated IKH calls, which attracted 20 proposals, including international applicants. Ten of these are planned as two- to three-year projects, reflecting IKH's emphasis on sustained interdisciplinary collaboration. Representative research themes include non-destructive analysis of bronze artifacts from the *Kofun* period, and of paint film samples related to the reconstruction of *Shuri* Castle, highlighting Ryukyu cultural heritage.

Building on this GIMRT-based collaboration, IKH has developed the Comprehensive Bronze Mirror Project at IMR. Drawing on IMR's long-standing strengths in materials science and analytical infrastructure, the project builds upon accumulated archaeological knowledge while introducing analytical perspectives from materials science, integrating non-destructive imaging, compositional analysis, and microstructural characterization (Fig. 1 and 2) [1]. Research questions guide the selection and integration of analytical methods, aiming to reveal previously inaccessible information embedded in bronze mirrors, thereby advancing their historical interpretation.

IKH also promotes interdisciplinary collaboration through two dedicated online research units: the Metal Archaeological Material Analysis Unit and the Quantum & Optical Non-Destructive Analysis Unit. These sessions connect humanities researchers, materials scientists, and facility operators to discuss techniques such as X-ray CT, EDS, EMPA, and neutron diffraction, building trust across disciplines and enhancing shared analytical capabilities.

Fig. 1 (Left) Bronze Mirror, Late Former Han period (early 1st century BCE). (Right) Prompt gamma-ray compositional analysis (PGA) at JRR-3.

Fig. 2 (Left) Electrical conductivity test of a bronze mirror. (Right) SEM–EDS analysis of a small bronze mirror in the Comprehensive Bronze Mirror Project at IMR.

In addition, IKH published an interdisciplinary casebook that compiles 39 research cases from the past decade, revealing the hidden histories of cultural heritage and promoting engagement with materials science.

In October 2025, IKH held its sixth interdisciplinary research meeting at Fukui Prefectural University and the Fukui Prefectural Dinosaur Museum, bringing together more than 100 participants and combining specialist presentations with a public lecture session.

Through these research, coordination, and outreach activities, IKH continues to serve as a bridge between the humanities and materials science, contributing to methodological innovation and a deeper understanding of cultural and natural heritage.

References

[1] M. Fujita, et al. "Revealing the Invisible: Materials Science Illuminating Archaeometallurgy", The international conference on "the Beginnings of the Use of Metals and Alloys," Sep. 2025.

Masaki Fujita (Head of Innovative Knowledge Hub for Humanities and Materials Science)
The Liaison for Innovative Knowledge Hub for Humanities and Materials Science
E-mail: imr-ikh@grp.tohoku.ac.jp
URL: https://ikh.imr.tohoku.ac.jp/

Editors

Public Relations Editorial Committee
Public Relations Office

Design

HOKUTO Corporation

Organization

Institute for Materials Research
Tohoku University
2-1-1 Katahira, Aoba-ku, Sendai 980-8577, Japan
Tel. +81-(0)22-215-2144 Fax. +81-(0)22-215-2482

URL: https://www.imr.tohoku.ac.jp/
E-mail: pro-adm.imr@grp.tohoku.ac.jp

The latest issue and back issues of KRH are available here.

The affiliations and positions are as of the time of writing.

東北大学 金属材料研究所
Institute for Materials Research
Tohoku University
2-1-1 Katahira, Aoba-ku
Sendai 980-8577, Japan
https://www.imr.tohoku.ac.jp/